Cell Reports

Article

Huygens synchronization of medial septal pacemaker neurons generates hippocampal theta oscillation

Graphical abstract

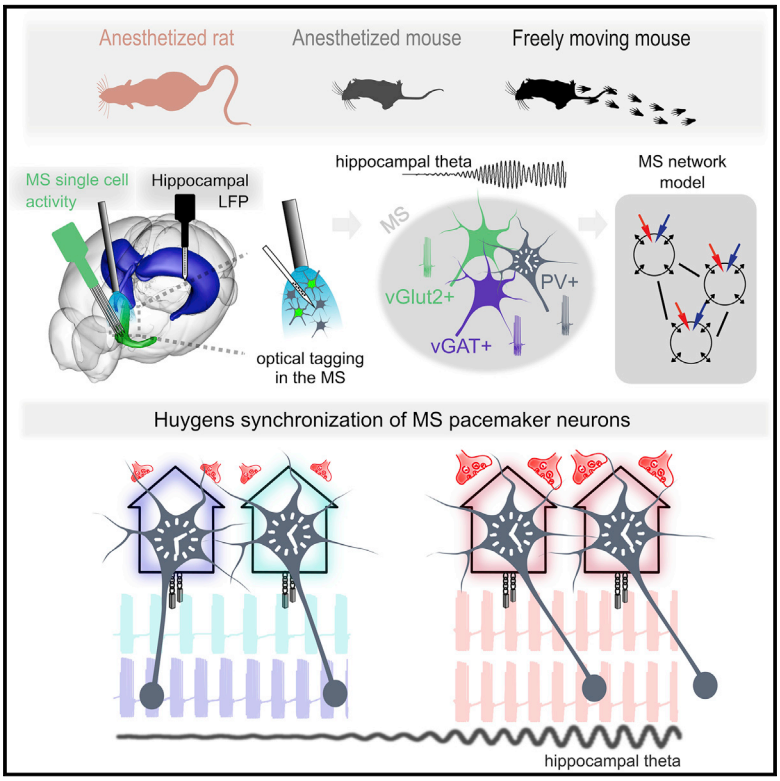

Highlights

- MS pacemakers show Huygens synchronization
- MS pacemakers are parvalbumin-expressing GABAergic neurons
- MS glutamatergic neurons provide tonic excitation sufficient to induce theta
- A network model of a homogeneous GABAergic population reproduces experimental data

Authors

Barnabás Kocsis, Sergio Martínez-Bellver, Richárd Fiáth, ..., Szabolcs Káli, Viktor Varga, Balázs Hangya

Correspondence

hangya.balazs@koki.hu

In brief

How medial septal (MS) neurons synchronize to generate hippocampal theta oscillation is not well understood. Kocsis et al. find that MS GABAergic neurons synchronize their individual rhythmicity frequencies, similar to coupled pendulum clocks, while MS glutamatergic neurons provide tonic excitatory drive to the pacemaker network sufficient to induce theta.

Kocsis et al., 2022, Cell Reports *40*, 111149
August 2, 2022
https://doi.org/10.1016/j.celrep.2022.111149

CellPress

Cell Reports

CellPress
OPEN ACCESS

Article

Huygens synchronization of medial septal pacemaker neurons generates hippocampal theta oscillation

Barnabás Kocsis,[1,2,3] Sergio Martínez-Bellver,[1,4] Richárd Fiáth,[2,5] Andor Domonkos,[6] Katalin Sviatkó,[1,7] Dániel Schlingloff,[1] Péter Barthó,[8] Tamás F. Freund,[6] István Ulbert,[2,5] Szabolcs Káli,[6] Viktor Varga,[6,9] and Balázs Hangya[1,10,*]

[1]Lendület Laboratory of Systems Neuroscience, Institute of Experimental Medicine, 1083 Budapest, Hungary
[2]Institute of Cognitive Neuroscience and Psychology, Research Centre for Natural Sciences, 1117 Budapest, Hungary
[3]Roska Tamás Doctoral School of Sciences and Technology, Faculty of Information Technology and Bionics, Pázmány Péter Catholic University, 1083 Budapest, Hungary
[4]Department of Anatomy and Human Embryology, Faculty of Medicine and Odontology, University of Valencia, 46010 Valencia, Spain
[5]Faculty of Information Technology and Bionics, Pázmány Péter Catholic University, 1083 Budapest, Hungary
[6]Cerebral Cortex Research Group, Institute of Experimental Medicine, 1083 Budapest, Hungary
[7]János Szentágothai Doctoral School of Neurosciences, Semmelweis University, 1085 Budapest, Hungary
[8]Sleep Oscillations Research Group, Research Centre for Natural Sciences, 1117 Budapest, Hungary
[9]Subcortical Modulation Research Group, Institute of Experimental Medicine, 1083 Budapest, Hungary
[10]Lead contact
*Correspondence: hangya.balazs@koki.hu
https://doi.org/10.1016/j.celrep.2022.111149

SUMMARY

Episodic learning and memory retrieval are dependent on hippocampal theta oscillation, thought to rely on the GABAergic network of the medial septum (MS). To test how this network achieves theta synchrony, we recorded MS neurons and hippocampal local field potential simultaneously in anesthetized and awake mice and rats. We show that MS pacemakers synchronize their individual rhythmicity frequencies, akin to coupled pendulum clocks as observed by Huygens. We optogenetically identified them as parvalbumin-expressing GABAergic neurons, while MS glutamatergic neurons provide tonic excitation sufficient to induce theta. In accordance, waxing and waning tonic excitation is sufficient to toggle between theta and non-theta states in a network model of single-compartment inhibitory pacemaker neurons. These results provide experimental and theoretical support to a frequency-synchronization mechanism for pacing hippocampal theta, which may serve as an inspirational prototype for synchronization processes in the central nervous system from Nematoda to Arthropoda to Chordate and Vertebrate phyla.

INTRODUCTION

Exploratory behaviors are accompanied by a 4–12 Hz theta oscillation in the hippocampus of rodents, carnivores, and primates, including humans (Buzsáki, 2002; Buzsáki and Moser, 2013; Kahana et al., 1999; Rutishauser et al., 2010). This theta oscillation provides a temporal reference signal for hippocampal networks, which is crucial for episodic learning and memory retrieval (Buzsáki, 2006). GABAergic neurons of the medial septum (MS) have been identified as putative pacemakers of hippocampal theta rhythms (Freund and Antal, 1988; Hangya et al., 2009; Petsche et al., 1962; Yoder and Pang, 2005). However, the mode of theta-frequency synchronization within the septal GABAergic network has not been tested experimentally.

Theoretical studies proposed that individual pacemaker neurons may oscillate at different frequencies and synchronize in the frequency domain upon increased depolarizing input (Ujfalussy and Kiss, 2006; Wang, 2002), a mechanism termed ''Huygens synchronization'' in the physics of coupled oscillators (Oliveira and Melo, 2015; Ramirez et al., 2016). Two influential models assumed the presence of two separate GABAergic populations that inhibit each other through a so-called ping-pong mechanism, either within the MS network (Cutsuridis and Poirazi, 2015; Ujfalussy and Kiss, 2006) or involving the hippocampo-septal GABAergic projection neurons (Wang, 2002). Theta amplitude modulation through increased MS firing rates was proposed as a direct layer of control (Bland et al., 1996; Denham and Borisyuk, 2000; Tokuda et al., 2019), whereas a change in MS bursting patterns could also impact theta generation (Joshi et al., 2017; Simon et al., 2006; Sotty et al., 2003). The role of the hyperpolarization-activated and cyclic nucleotide-gated (HCN) channels was emphasized as a part of the potential underlying ionic mechanisms (Kocsis and Li, 2004; Varga et al., 2008). However, beside frequency synchronization, other mechanisms are also plausible, including synchronization in the phase domain without changes in oscillation frequency (Borhegyi et al., 2004; Ujfalussy and Kiss, 2006). Additionally, little is known about the exact role of different MS cell types in theta generation (Lee et al., 1994; Robinson et al., 2016; Vandecasteele et al., 2014).

Therefore, we investigated potential theta generation mechanisms experimentally by recording single neurons from the medial septum, with concurrent local field potentials (LFP) from the hippocampus using multichannel silicon electrode arrays. To address the generality of results across theta oscillations observed in awake or anesthetized rodents (Kramis et al., 1975; Stewart and Fox, 1989), we obtained three datasets: from urethane-anesthetized rats, urethane-anesthetized mice, and awake, drug-free mice. We found that hippocampal theta onset was accompanied by Huygens (frequency) synchronization of MS pacemaker neurons otherwise rhythmic at more distinct frequencies in the theta range. We confirmed the pacemaker role of parvalbumin (PV)-expressing GABAergic neurons (Freund and Antal, 1988; Hangya et al., 2009; Varga et al., 2008) by optogenetic tagging (Kvitsiani et al., 2013; Lima et al., 2009), whereas glutamatergic neurons showed strong firing rate increase during theta without much rhythmicity, suggesting they may contribute to the theta-associated increase of tonic drive to the pacemakers (Ford et al., 1989; Green and Arduini, 1954; Oddie et al., 1996; Vandecasteele et al., 2014; Yang et al., 2014). Indeed, optogenetic stimulation of MS glutamatergic neurons induced theta oscillation in the CA1. These results were consistent with a circuit model of the MS in which a network of inhibitory neurons was capable of synchronizing and desynchronizing in the frequency domain upon changing levels of tonic excitatory input.

RESULTS

Recording MS and hippocampal data in three rodent models of theta oscillations

Hippocampal theta oscillations have been investigated in both urethane-anesthetized and awake rodents (Borhegyi et al., 2004; Buzsáki, 2002; Klausberger and Somogyi, 2008; Kramis et al., 1975; Mikulovic et al., 2018; Stewart and Fox, 1989). To explore the commonalities and differences across different theta model systems, we collected three independent datasets (Figure 1). We recorded multiple single neurons from the MS using silicon probes from anesthetized rats (n = 903 neurons from n = 7 rats; 416 and 636 neurons active during both theta and non-theta states or at least one of them, respectively; Figure S1A), anesthetized mice (n = 1,155 neurons from n = 11 mice; 617 and 950 active during both or at least one of the states; Figures 1A–1D) and awake mice (n = 312 neurons from n = 4 mice; 265 and 289 active during both or at least one of the states; Figure S1B). Simultaneously, we recorded LFP from all layers of the dorsal CA1 area of the hippocampus using linear silicon probe electrodes (Figure 1E). We detected the hippocampal layers based on combined information from histology and theta phase reversal (Buzsáki, 2006; Buzsaki et al., 1986; Green et al., 1960) and used the large amplitude stratum radiatum/lacunosum-moleculare signal for detecting theta epochs (Figure S1C) (Buzsáki, 2002). Theta frequency boundaries were defined specifically for the three types of recordings based on LFP spectra, confirming the known observation of slower oscillations under urethane anesthesia (Borhegyi et al., 2004; Varga et al., 2008) (Figure 1F). Theta segments were detected based on the theta/delta spectral ratio (McNamara et al., 2014; Wikenheiser and Redish, 2013) (Figures 1G and 1H).

Putative pacemaker neurons show constitutive theta-rhythmic activity

We developed an unbiased method to identify functional MS neuron classes based on their rhythmic firing properties. Theta and delta rhythmicity indices were defined by the normalized autocorrelation peak in the respective frequency bands, and significant rhythmic activity was tested against bootstrap distributions generated from simulated Poisson neurons that were matched with MS neurons in their firing rates ($p < 0.05$, bootstrap test; Figure S2; STAR Methods).

We found that a subpopulation of MS neurons showed theta-rhythmic bursting activity both when theta oscillation was present and when it was absent in the CA1 (Figure 2A). These neurons showed prominent theta oscillations in their autocorrelograms (Figures 2B–2D) and strong phase locking to CA1 theta oscillation, but no strong phase relationship with hippocampal delta band activity during non-theta episodes (Figures 2E–2G). This constitutively theta-rhythmic population, often considered as "putative pacemaker neurons" of theta oscillation (Borhegyi et al., 2004; Ford et al., 1989; Hangya et al., 2009; Stewart and Fox, 1989; Varga et al., 2008) was found in anesthetized rats (n = 29/416), anesthetized mice (n = 47/617), and freely moving mice (n = 35/265; note that these numbers represent conservative estimates based on significant rhythmicity) (Figure S3, Figure S4).

We confirmed the presence of two separate clusters of neurons that showed anti-phase preference to hippocampal theta in anesthetized rats (Akaike information criterion values for the unimodal, bimodal, and trimodal distributions were 109.08, 103.19, and 108.98, respectively; Bayesian information criterion values were 111.81, 110.03, and 119.92), as reported previously (Borhegyi et al., 2004; Varga et al., 2008). Although a similar tendency could be observed in mice, we did not find statistical support for a bimodal distribution based on our samples (see STAR Methods; Table S1).

Putative "follower," theta-skipping, and tonically active MS neurons

A considerable MS population reflected (followed) the ongoing activity of the septo-hippocampal network. These neurons were theta-rhythmic during hippocampal theta oscillation but not when it was absent, often phase locked to both theta and delta band oscillations. In anesthetized rats, many of these neurons showed slow rhythmic activity at delta frequencies in the absence of hippocampal theta (Figure 3; Figure S5), while in mice, these follower neurons were mostly non-rhythmic or slow firing in non-theta states ("theta follower neurons") (Figures S6–S8; Table S1). Some neurons exhibited follower activity only in the non-theta state, remaining non-rhythmic or silent during hippocampal theta.

A subpopulation of MS neurons, identified previously as "theta-skipping," showed slow rhythmic activity regardless of whether theta oscillation was present in CA1 (Figure S9). While some of these neurons doubled their rhythmic frequency at theta onset (but still in the delta range), many cells of this population maintained a constant slow rhythmicity, often firing regularly in every second theta cycle. Interestingly, while this group was rather prominent in anesthetized rats, these cells were only rarely

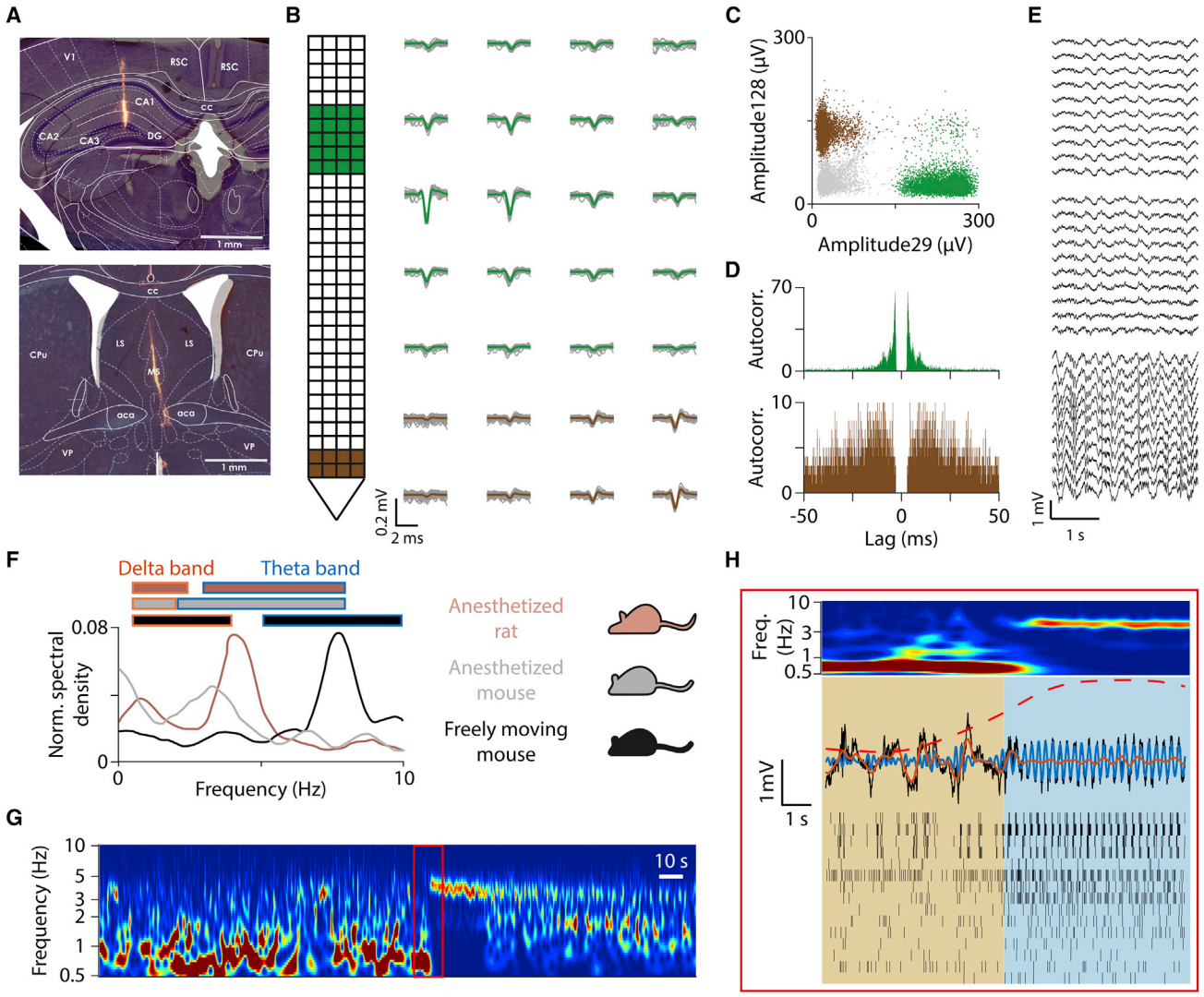

Figure 1. Dual recording of hippocampal LFP and single neuron activity from the medial septum

(A) Histology of the silicon probe tracks in the mouse hippocampus (top) and medial septum (bottom). Nissl-staining; red, DiI. See also Figure S1 for histology in rats.

(B) MS single units were collected using a 128-channel silicon probe in anesthetized mice (see STAR Methods). Example spike waveforms for two neurons are shown for the channels marked on the schematic representation of the probe (green and brown, average waveforms; grey, 100 randomly selected individual spikes).

(C) Amplitudes (peak-to-valley) on selected channels show clear separation of the example cells.

(D) Autocorrelograms of the example neurons.

(E) Hippocampal LFP was collected concurrently using a linear silicon probe. A 3-second-long example recording is shown (two broken channels were removed).

(F) We collected data from three rodent models of theta oscillations: urethane-anesthetized rats (brown), urethane-anesthetized mice (grey), and freely moving mice (black). Representative Fourier spectra of hippocampal LFP recordings from the three model systems. Theta and delta band boundaries were determined based on Fourier spectra of hippocampal LFPs for each model separately, indicated by color-coded horizontal bars on top.

(G) Representative hippocampal LFP wavelet spectrogram from an anesthetized rat recording.

(H) Top, theta onset is enlarged from (G). Middle, raw LFP (black), LFP filtered in the theta (blue) and delta frequency band (orange), and theta-delta power ratio (dashed line). Bottom, raster plot of individual units (n = 15) recorded from the medial septum concurrently. Note the change in network activity at theta onset.

found in mice, revealing species-specific differences in the MS theta generation network (anesthetized rats, 48/416; anesthetized mice, 4/617; freely moving mice, 1/265; Table S1).

Finally, a group of MS cells showed regular rhythmic firing patterns resembling those of striatal cholinergic interneurons (Inokawa et al., 2010); therefore, we called this MS group "tonically active neurons" (Figures S10A–S10D). Although these neurons fired rhythmically with a frequency in the theta band (Figures S10E–S10I), they showed little to no overall phase locking to hippocampal activity (Figures S10J–S10K), typically exhibiting rhythmicity at slightly higher frequencies than ongoing CA1 theta oscillation (based on autocorrelation peak, median ± standard

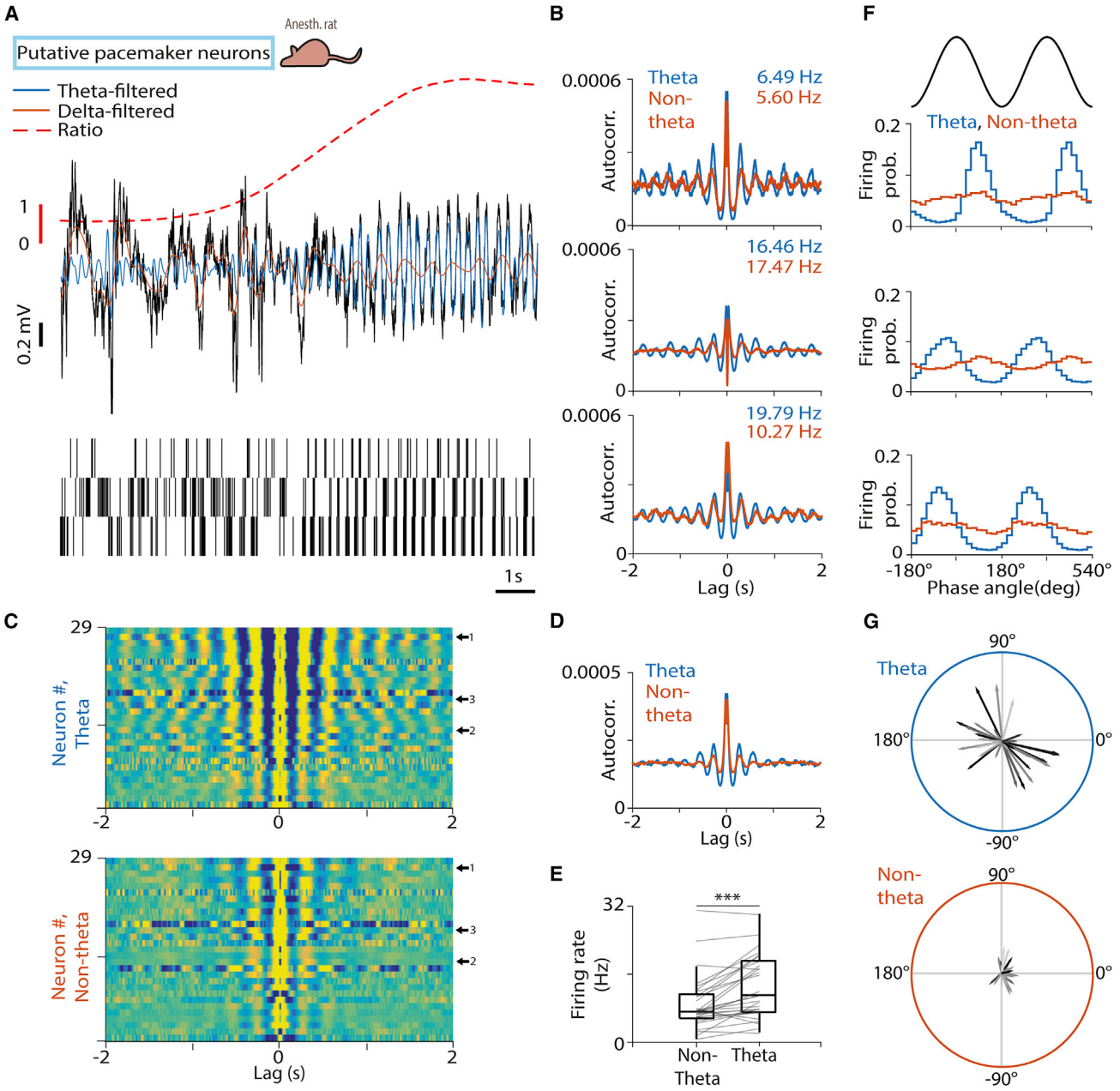

Figure 2. Putative pacemaker neurons of the MS

(A) Top, black, raw LFP from the CA1 shows a delta-to-theta state transition. Orange, LFP filtered in the delta band; blue, LFP filtered in the theta band; dashed, theta-delta amplitude ratio. Bottom, spike raster of three examples of putative pacemaker neurons from the same recording session. Recordings are from urethane-anesthetized rats; see Figures S3 and S4 for the anesthetized and awake mouse recordings.

(B) Autocorrelograms of the three example neurons in (A). Numbers indicate average firing rates during theta and non-theta segments.

(C) Autocorrelograms of all putative pacemaker neurons during theta (top) and non-theta (bottom) segments. Arrows indicate the example neurons.

(D) Average autocorrelogram of all putative pacemaker neurons.

(E) Firing rates of putative pacemaker neurons during non-theta and theta segments. Boxes and whiskers represent interquartile ranges and non-outlier ranges, respectively. Lines correspond to individual neurons. Firing rate was significantly higher during theta (***$p < 0.001$; $p = 1.04 \times 10^{-4}$, $W = 397$, $n = 29$, Wilcoxon signed-rank test).

(F) Phase histogram of the example neurons in (A) relative to delta (orange) and theta (blue) oscillations. Two oscillatory cycles are shown.

(G) Phase-locking of all putative pacemaker neurons to theta (top) and delta (bottom) oscillation in polar coordinates. Angle, circular phase; length, mean vector length; greyscale corresponds to average firing rate (black, higher firing rate). Note that neurons formed two opposite phase clusters during theta, whereas phase-locking strength to delta oscillations was low for putative pacemaker neurons.

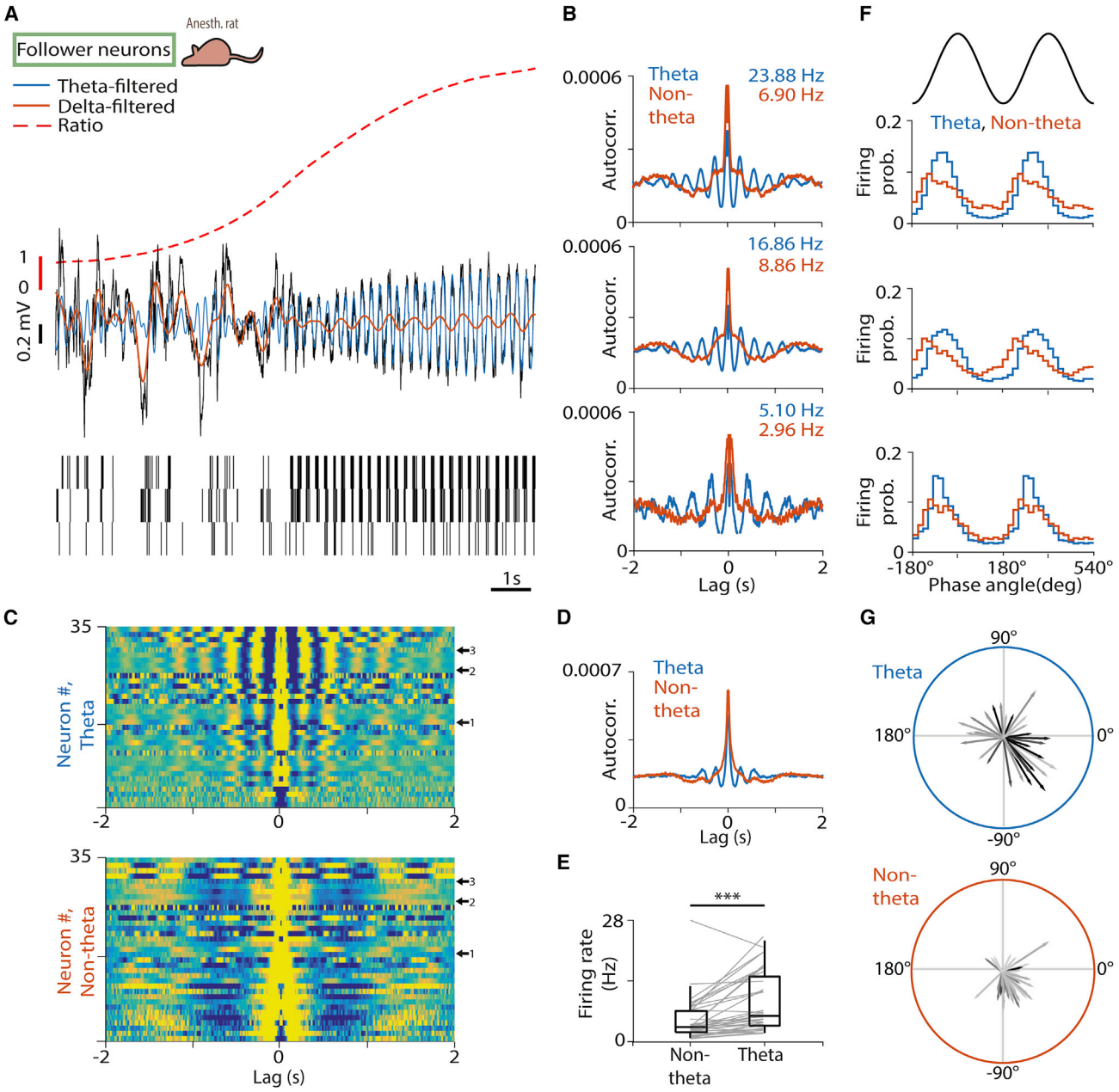

Figure 3. Follower MS neurons

(A) Top, black, raw LFP from the CA1 shows a delta-to-theta state transition. Orange, LFP filtered in the delta band; blue, LFP filtered in the theta band; dashed, theta-delta amplitude ratio. Bottom, spike raster of three example neurons from the same recording session. Follower neurons showed delta-rhythmic activity during non-theta epochs and theta-rhythmic activity during theta epochs in urethane-anesthetized rats. See Figure S6 for mouse recordings.

(B) Autocorrelograms of the three example neurons in (A). Numbers indicate average firing rates during theta and non-theta segments.

(C) Autocorrelograms of all follower neurons during theta (top) and non-theta (bottom) segments. Arrows indicate the example neurons.

(D) Average autocorrelogram of all follower neurons.

(E) Firing rates of follower neurons during non-theta and theta segments. Boxes and whiskers represent interquartile ranges and non-outlier ranges, respectively. Lines correspond to individual neurons. Firing rate was significantly higher during theta (***$p < 0.001$; $p = 1.65 \times 10^{-5}$, $W = 578$, $n = 35$, Wilcoxon signed-rank test).

(F) Phase histogram of the example neurons in (A) relative to delta (orange) and theta (blue) oscillations. Two oscillatory cycles are shown.

(G) Phase locking of all follower neurons to theta (top) and delta (bottom) oscillation in polar coordinates. Angle, circular phase; length, mean vector length; greyscale corresponds to average firing rate (black, higher firing rate). Many of these neurons were phase-locked to both hippocampal oscillations.

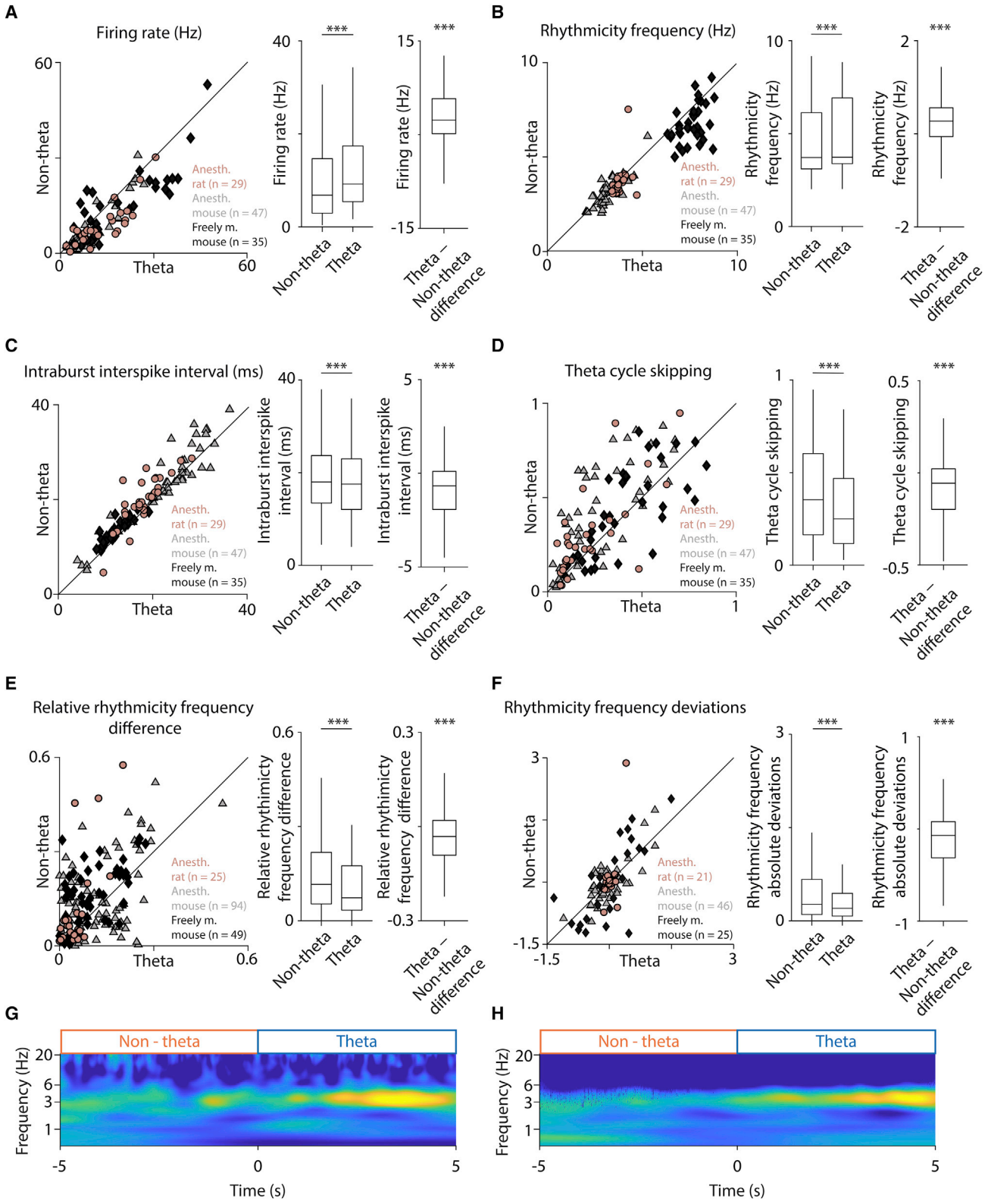

Figure 4. Septal pacemakers synchronize their burst frequencies

(A) Firing rates of MS putative pacemakers were higher during theta oscillation then during non-theta segments. Left, scatter plot shows the firing rate of all putative pacemaker neurons, color coded according to the rodent theta models. Middle and right, box-whisker plots showing statistics on pooled data

(legend continued on next page)

error of the median, 5.68 ± 0.34, 4.29 ± 0.41, and 8.40 ± 0.37 Hz during theta segments in anesthetized rats, anesthetized mice, and freely moving mice, respectively). They did not show the long bursts with 20- to 50-ms interspike intervals (ISIs) known to be characteristic of the putative pacemaker group, but some of them occasionally fired short, fast bursts of action potentials (ISI < 15 ms; Figures S10A–S10D). They were found in all three rodent theta models tested (anesthetized rats, 18/416; anesthetized mice, 49/617; freely moving mice, 8/265) (Figures S11 and S12A–S12G). These neurons also showed a firing rate change during theta oscillation. Interestingly, however, while their firing rate decreased at theta onset in rats (15/18 neurons), previously coined as a "theta-OFF" pattern (Ford et al., 1989) (Figure S10I), they exhibited a theta-associated firing rate increase in mice, both anesthetized (34/49 neurons) and awake (8/8 neurons) (Figures S11E and S12E; Table S1).

Together with those cells that did not exhibit any rhythmic activity according to our conservative rhythmicity analysis, the above-described groups of MS neurons constitute the entire MS population (Figure S12H; Table S2).

Septal pacemakers synchronize their burst frequencies

To gain information on the neural synchronies between the above-described groups, we calculated pairwise cross-correlations for pairs of MS cells (n = 527 pairs in anesthetized rats). We found that during non-theta segments, follower neurons showed strong synchrony within each other, but also with putative pacemaker neurons (Figure S13). This remained consistent across theta and non-theta segments, while the putative pacemaker neurons became the most synchronous group in theta state. Tonically active neurons showed lower levels of synchrony within each other and with putative pacemakers, while they expressed moderate correlations with follower neurons. Therefore, we reasoned that theta-rhythmic putative pacemaker and follower neurons likely participate in the MS theta generating mechanisms, unlike tonically active neurons.

We found that, during CA1 theta, putative pacemakers showed an increased firing rate and somewhat higher rhythmicity frequency as measured by the first peak in their autocorrelograms, arguing for a stronger excitatory drive during theta (Figures 4A and 4B). Interestingly, we only found moderate changes in burst parameters, suggesting that the bursting mechanisms of MS pacemakers are mostly intrinsic and show only slight modulation with changing network states (Figure 4C). Since the change in burst parameters and rhythmicity frequency seemed too small to account for the observed elevated firing rate, we argued that putative pacemakers should be skipping more theta cycles during non-theta states. We confirmed this by calculating the proportion of cycles skipped during non-theta and theta activity (Figure 4D).

Next, we analyzed the pairs of putative pacemakers further to address how the synchrony of these neurons changes during hippocampal theta oscillation. Based on theoretical work, we hypothesized that pacemaker neurons may synchronize their frequencies, thus increasing constructive interference across individual oscillators, providing a stronger theta-rhythmic output toward the hippocampus (Ramirez et al., 2016; Ujfalussy and Kiss, 2006; Wang, 2002; Willms et al., 2017). This would imply that pairwise differences in the rhythmicity frequency of putative pacemakers decrease during theta oscillation compared with non-theta episodes. Indeed, we found smaller differences in individual theta frequencies when hippocampal theta was present when we pooled all pacemaker pairs from the three datasets (Figure 4E). This difference was significant for anesthetized rats and freely moving mice, and marginally significant when only anesthetized mice were considered (Table S3). This frequency synchronization was detected after normalizing the relative frequency difference to the individual frequencies of the tested neurons; thus, a change in the individual theta frequencies could not account for this effect.

If differences across rhythmicity frequencies decrease during theta, one also expects rhythmicity frequencies across the putative pacemaker population to converge to a tighter distribution. We tested this by comparing the absolute deviation of rhythmicity frequencies from their mean during theta and non-theta segments and found a larger spread in non-theta state (Figure 4F). Additionally, we visualized the pacemaker synchronization process by calculating wavelet coherence among putative

(***$p < 0.001$; $p = 1.402 \times 10^{-9}$, W = 5166, n = 111, Wilcoxon signed-rank test). See Table S3 for statistics on the three datasets separately. All box-whisker plots show median, interquartile range and non-outlier range in this figure.

(B) Left, scatter plot of rhythmicity frequency of putative pacemakers measured by the time lag of the first autocorrelation peak in the theta band. Middle and right, statistics on pooled data indicated higher rhythmicity frequency during hippocampal theta (***$p < 0.001$; $p = 2.64 \times 10^{-7}$, W = 4857.5, n = 111, Wilcoxon signed-rank test).

(C) Left, scatter plot of average intraburst ISIs for putative pacemaker neurons. Middle and right, the moderate decrease of ISIs during theta oscillation indicates a slight elevation of intraburst frequency (***$p < 0.001$; $p = 7.336 \times 10^{-5}$, W = 1275.5, n = 111, Wilcoxon signed-rank test).

(D) Left, scatter plot of the ratio of skipped theta cycles of putative pacemakers during non-theta and theta segments. Middle and right, statistics on pooled data indicated that putative pacemaker neurons skipped more theta cycles during non-theta segments (***$p < 0.001$; $p = 3.021 \times 10^{-6}$, W = 1521, n = 111, Wilcoxon signed-rank test).

(E) Left, scatter plot of relative frequency difference of individual pacemaker neurons for simultaneously recorded pairs, normalized to the larger of the frequencies. Middle and right, statistics on pooled data indicated that individual pacemakers became more similar in frequency during theta oscillation (***$p < 0.001$; $p = 3.17 \times 10^{-6}$, W = 4156, n = 168, Wilcoxon signed-rank test).

(F) Left, deviation from the session mean rhythmicity frequency during theta vs. non-theta segments for putative pacemaker neurons (sessions in which at least two putative pacemakers were co-recorded are included). Middle and right, statistics on pooled data indicated that the absolute deviation from the mean rhythmicity frequency was significantly larger during non-theta segments (***$p < 0.001$; $p = 4.189 \times 10^{-4}$, W = 1233, n = 92, Wilcoxon signed-rank test).

(G) Mean wavelet coherence spectrogram of an example putative pacemaker neuron pair (spike trains were convolved with a 50-ms Gaussian window, from anesthetized rat) averaged around non-theta to theta transitions.

(H) Mean wavelet coherence spectrogram averaged across pairs of putative pacemaker neurons recorded in urethane-anesthetized rats (time 0 corresponds to non-theta to theta transitions; sessions in which at least two putative pacemakers were co-recorded are included, n = 25 pairs).

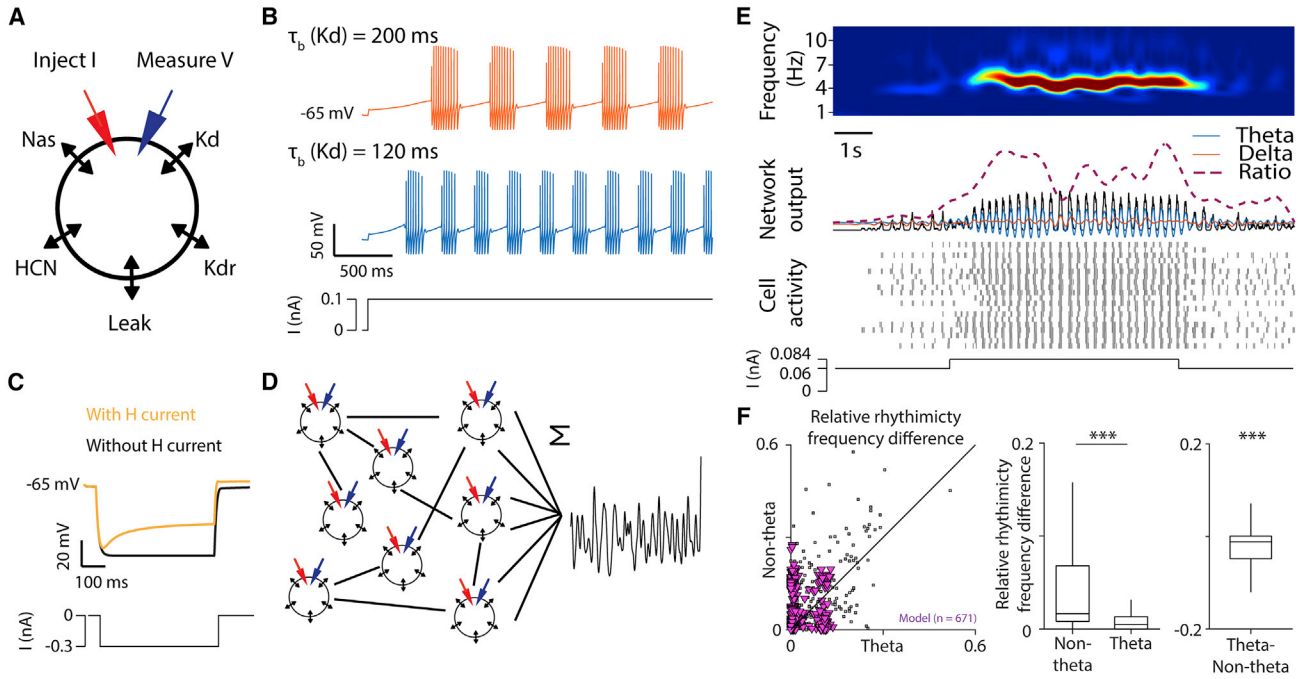

Figure 5. A simple conductance-based network model of the MS pacemaker circuit is capable of theta-synchronization upon tonic excitation

(A) Schematic of the single-compartment model neuron. The inhibitory neuron was equipped with transient sodium (Nas), slowly inactivating D-type potassium (Kd), delayed rectifier potassium (Kdr), HCN channels and passive leak channels. An electrode delivering current is attached to the cell.

(B) Rhythmicity frequency of the model neuron can be controlled by the τ_b(Kd) inactivation time constant. Slower inactivation (200 ms) also increases burst length.

(C) Adding H current caused a sag response to hyperpolarizing current, similar to MS GABAergic neurons reported in the literature (see, e.g., Figure 1C in Xu et al. [2004]). The moderate rebound effect did not induce rebound spikes.

(D) Schematics of the network. Twenty model cells were connected with simulated GABA-A-mediated inhibitory synapses. Spike trains were summed and convolved with a 50-ms Gaussian window to model network output.

(E) Simulation of network behavior (60% connection rate; 7-ms synaptic delay, 3-nS mean synaptic strength; 2-ms synaptic decay; 10% variance for the latter three synaptic parameters; 60-pA mean baseline stimulation with 10% variance). Neurons synchronized in the theta frequency band in response to a tonic increase of stimulation and desynchronized when stimulation was reset to baseline. (Increased excitation was applied with jittered onset latency to avoid synchronous phase reset; see STAR Methods.) Top, wavelet spectrogram of network output. Middle, network output (black, raw; blue, filtered in the theta band; orange, filtered in the delta band; dashed, theta-delta ratio) and simulated spike raster. Bottom, injected current.

(F) Left, scatter plot of relative frequency difference of simultaneous pairs of pacemaker neurons, normalized to the larger of the frequencies; real data in black (three datasets pooled, see Figure 4E), model data overlaid in magenta. Middle and right, statistics indicated that individual model pacemakers became more similar in frequency during theta (***$p < 0.001$; $p = 2.20 \times 10^{-30}$, W = 51519, n = 671, Wilcoxon signed-rank test). Box-whisker plots show median, interquartile range and non-outlier range.

pacemaker pairs. This analysis also indicated greater coherence in a narrow frequency band among putative pacemakers during theta (Figures 4G and 4H). Thus, these analyses confirmed our prediction that the theta-rhythmic population converges to a tighter rhythmicity frequency distribution after theta onset.

Network model of the medial septum confirms frequency (Huygens) synchronization mechanism

Our neural data suggested that increased tonic excitation led to higher firing rates and frequency synchronization in putative pacemakers that resulted in a strong theta-modulated output. To test if a simple network model of a homogeneous MS pacemaker population could produce these dynamics, we simulated MS neurons based on a minimalistic single-compartment conductance-based model constructed to produce fast spiking burst dynamics (Golomb et al., 2007) (Figure 5A). The model neuron expressed rhythmic discharges upon current injection with a rhythmicity frequency in the delta-theta range, controlled by the inactivation time constant of a slowly inactivating D-type potassium channel (Figure 5B). Septal pacemaker neurons are known to express strong H-currents (Kocsis and Li, 2004; Xu et al., 2004); hence, we also included an HCN channel in the model, which successfully reproduced the previously reported H-current characteristics (Figure 5C).

Next, we built a network model by connecting the neurons with inhibitory synapses, simulating GABA-A receptor kinetics with a reversal potential at −70 mV that triggered fast inhibitory postsynaptic currents. All neurons received a non-rhythmic (“tonic”) somatic excitatory current to mimic the changing excitatory drive to the septal pacemaker population. To model the impact of the MS output on the hippocampal LFP, we convolved the averaged septal firing with a Gaussian kernel (Figure 5D). We found that, at low tonic excitation levels, the modelled septal output showed irregular activity with low levels of theta oscillation. Increasing

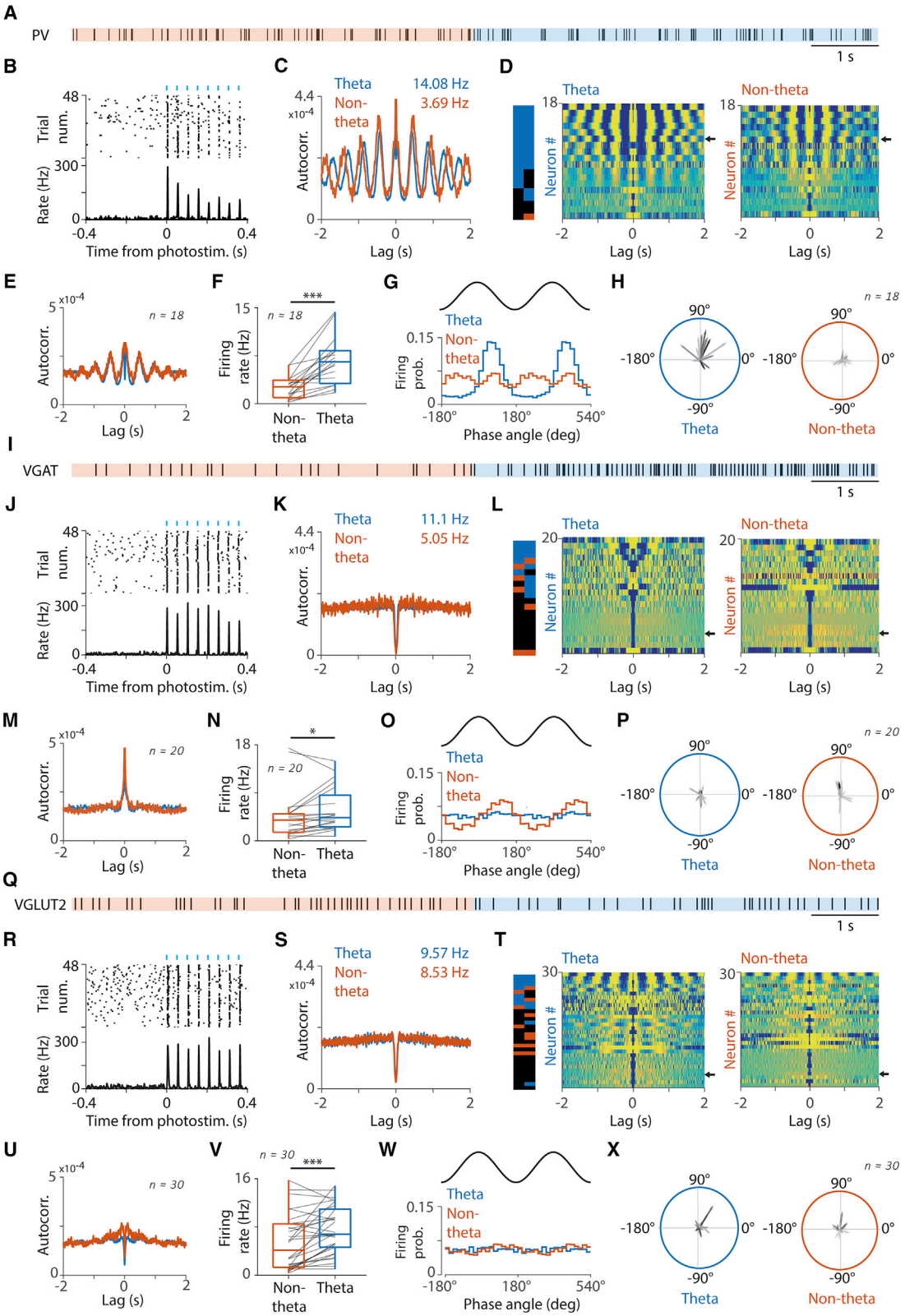

(legend on next page)

the tonic drive resulted in a strong theta oscillatory output, which returned to the irregular activity when the tonic current was decreased (Figure 5E). Thus, the level of non-rhythmic excitation could toggle the model pacemaker network between theta and non-theta output, as suggested earlier (Bland et al., 1996; Hajszan et al., 2004) and consistent with our neural recordings.

To test the robustness and parameter dependence of this finding, we systematically explored the parameter space (Figures S14A–S14E). We found a discrete maximum of the model's synchronization capabilities at a mean baseline excitation of around 60 pA, which was largely independent of the connectivity rate. Interestingly, very strong baseline excitation could result in a mirrored activity (decreased theta synchronization upon increased excitation owing to switching to a continuously firing mode, indicated by a synchronization score <0.5), sometimes also observed in anesthetized preparations. Fixing the baseline tonic excitation at the optimum, the model network was capable of synchronizing at a range of mean synaptic strength levels and connection rates.

This model allowed us to test whether a network of interconnected, minimalistic inhibitory MS units, without introducing specialized subpopulations and biased connectivity, exhibits the same frequency synchronization properties as we found in the septal network *in vivo*. To address this, we repeated the same battery of analyses on the model that we ran on the neural data (Figures S14F–S14K). We found that model neurons increased their firing rate in theta state (Figure S14F), accompanied by a slight increase in rhythmicity frequency (Figure S14G) and a strong decrease in theta skipping (Figure S14I), with a consistent but relatively small change in burst properties (Figure S14H). When we compared pairwise differences in pacemaker frequencies, we found a significant theta-associated decrease (Figure 5F), accompanied by a tightening of the rhythmicity frequency distribution (Figure S14K), suggesting the presence of a frequency synchronization mechanism.

Since a subset of putative pacemaker pairs showed stable anti-phasic firing patterns in urethane-anesthetized rats (Figures S14L–S14M), we tested whether the model also generated anti-phasic firing patterns. The analysis of pairwise cross-correlograms showed that in-phase synchrony dominated in most of the parameter space (Figures S14N–S14O), whereas we also found examples of anti-phasic synchronization (Figures S14P–S14S). This suggests that anti-phasic synchronization can occur in the model, although it is not necessary for theta synchronization, in accordance with Huygens synchronization theory.

Thus, the model behaved similarly to the rodent theta-generating networks, confirming that Huygens-type frequency synchronization might be a general mechanism operating in brain networks, similar to many mechanical systems.

Most PV-expressing GABAergic neurons are theta rhythmic, whereas MS glutamatergic neurons are "tonic theta ON"

Finally, to investigate the genetic and neurotransmitter identity of MS neurons, we performed optogenetic tagging in urethane-anesthetized mice in a separate set of experiments (Figures S15A–S15I). Theta oscillation was induced by tail pinch, and we performed theta detection and rhythmicity-based classification of MS neurons as above. We performed optogenetic stimulation in PV-Cre (n = 2), vesicular GABA transporter (VGAT)-Cre (n = 2) or VGluT2-Cre (n = 3) mice transduced by a Cre-dependent Channelrhodopsin (ChR2) construct injected in the MS to identify PV-expressing, GABAergic, and glutamatergic MS neurons, respectively (Gritti et al., 2006; Sotty et al., 2003).

We found that many PV-expressing neurons were theta rhythmic (Figures 6A–6H), and 9 of 18 neurons were characterized as putative pacemakers (Figure S15J). Surprisingly, GABAergic neurons as a population contained few theta-rhythmic neurons; instead, most VGAT+ MS neurons were non-rhythmic (Figures 6I–6P and S15J; n = 2/20 putative pacemakers). Anatomical studies showed that a subset of GABAergic MS neurons express PV (Gritti et al., 2003; Kiss et al., 1990; Unal et al., 2015; Yang et al., 2017; Zaborszky et al., 1999, 2012), suggesting that the subset of VGAT+ MS neurons that were rhythmic may have been PV expressing. These results suggest that PV expression marks the theta-generating population, confirming previous studies (Borhegyi et al., 2004; Freund, 1989; Varga et al., 2008). When we calculated the theta-associated change in relative frequency differences between pairs of putative pacemakers where at least one of the cells was tagged as PV+ (Figure S15K), we found similar frequency synchronization as shown for unlabeled pairs of putative pacemakers in Figure 4E and for model pacemaker neurons in Figure 5F.

Figure 6. Optogenetic identification of MS neuron types in anesthetized mice

(A) Example spike raster of a PV-expressing MS neuron during non-theta (orange) and theta (blue) segments.

(B) Raster plot (top) and corresponding peri-stimulus time histogram (bottom) of an example PV-expressing light-sensitive MS neuron aligned to the onset of 20 Hz photostimulation (blue ticks).

(C) Autocorrelograms of the example neuron during non-theta (orange) and theta (blue) segments. Numbers in the top right corner indicate average firing rate during non-theta (orange) and theta (blue).

(D) Autocorrelograms of all identified PV-expressing MS neurons, sorted by rhythmicity index. Left, color bar indicates significant theta-rhythmicity (blue) and delta-rhythmicity (orange) during theta (left) and non-theta (right) segments. Middle, autocorrelograms during theta segments. Right, autocorrelograms during non-theta segments. The arrows indicate the example neuron. Most PV-positive MS neurons were constitutively theta-bursting putative pacemakers.

(E) Average autocorrelogram of all identified PV-expressing MS neurons.

(F) Firing rate change between non-theta and theta segments of all identified PV-expressing MS neurons (***$p < 0.001$; $p = 2.33 \times 10^{-4}$, W = 170, n = 18, Wilcoxon signed-rank test).

(G) Phase-locking of the example neuron to delta (orange) and theta (blue) oscillations.

(H) Phase-locking of all identified PV-expressing MS neurons to theta (left) and delta (right) oscillations. Greyscale indicates average firing rate.

(I–P) Same as (A–H), but for VGAT-expressing MS neurons. In (N), *$p < 0.05$; $p = 3.66 \times 10^{-2}$, W = 161, n = 20, Wilcoxon signed-rank test.

(Q–X) Same as in (A–H), but for VGLUT2-expressing MS neurons. In (V), ***$p < 0.001$; $p = 8.94 \times 10^{-4}$, W = 394, n = 30, Wilcoxon signed-rank test.

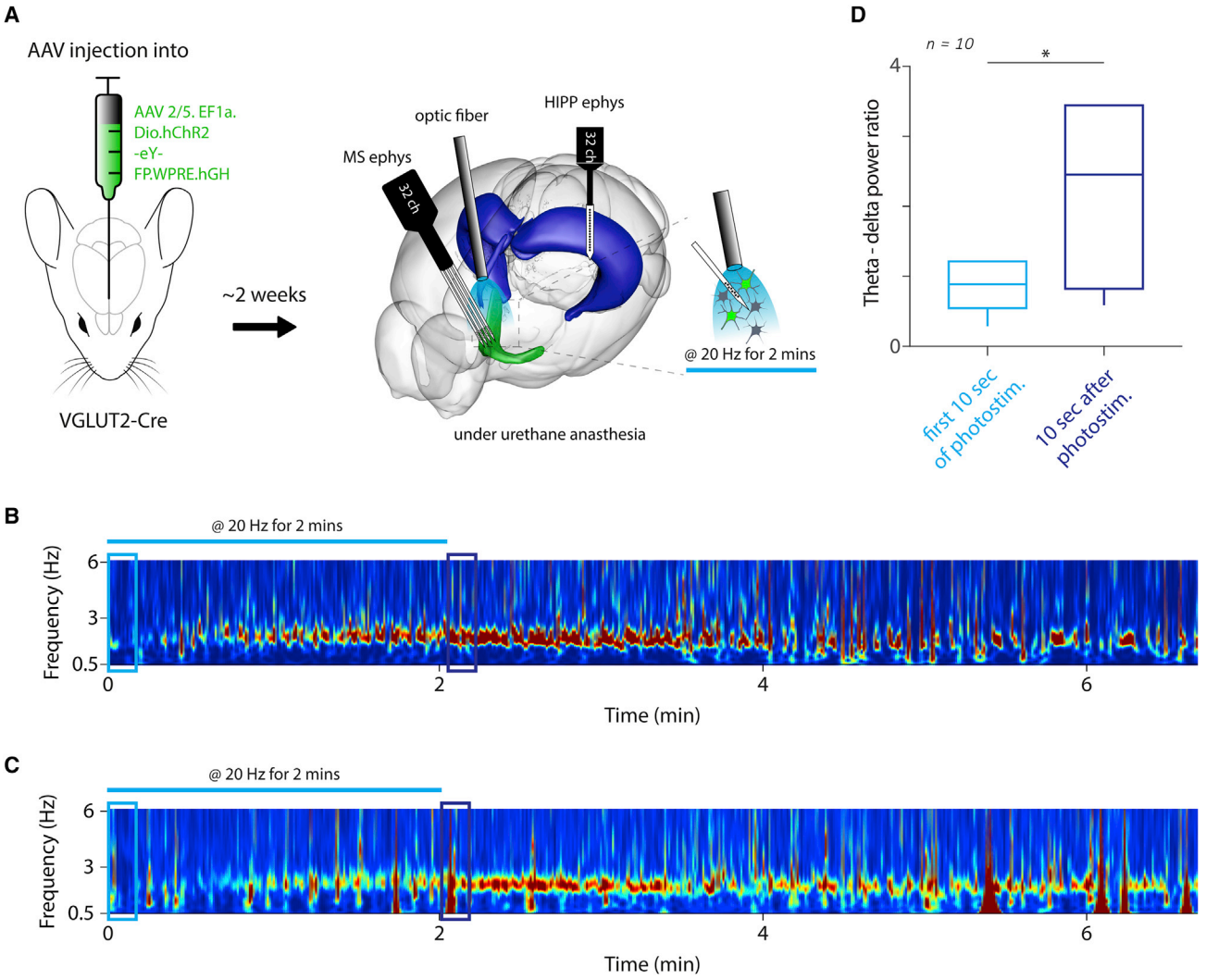

Figure 7. Optogenetic stimulation of MS glutamatergic neurons at 20 Hz generates theta oscillations in CA1

(A) Schematic of the experiment. VLGUT2-Cre mice were injected with AAV2/5.EF1a.Dio.hChR2-eYFP.WPRE.hGh in the MS and implanted with an optic fiber in the MS and silicon probes in the MS and CA1 in acute anesthetized experiments. Three-dimensional mouse brain adopted from Bakker et al. (2015).

(B) Wavelet spectrogram of an example CA1 LFP segment during and after 20-Hz stimulation of MS glutamatergic neurons. The photostimulation induced lasting theta oscillation. (Note the lower frequency of theta typical under anesthesia).

(C) Average of all recording sessions (n = 10) of 20 Hz glutamatergic stimulation).

(D) Box-whisker plot showing significant increase in theta-delta ratio upon glutamatergic stimulation. Median, interquartile range and non-outlier range are shown (*$p < 0.05$; $p = 3.71 \times 10^{-2}$, W = 7, n = 10, Wilcoxon signed-rank test).

The majority of optogenetically identified MS glutamatergic neurons showed a strong increase in the firing rate (fold increase median ± standard error of the median, 1.42 ± 0.34) without any theta rhythmicity during hippocampal theta state (Figures 6Q–6X, Figure S15J). Few glutamatergic neurons were theta-rhythmic, with 3 of 30 characterized as pacemakers. This identifies the MS glutamatergic population as tonic theta ON neurons (Ford et al., 1989).

Thus, local glutamatergic neurons may contribute to the increased excitatory drive to the MS pacemaker neurons during theta synchronization. To directly test this prediction, we analyzed CA1 LFP after 20 Hz stimulation of MS glutamatergic neurons in urethane-anesthetized VGLUT2-Cre mice (Figure 7A). Optogenetic stimulation induced hippocampal theta oscillation in most cases, reflected in the appearance of theta frequencies in the wavelet spectrogram of CA1 LFP recordings (Figures 7B and 7C), and a significant increase in the theta-delta ratio upon photostimulation (Figure 7D).

DISCUSSION

We categorized MS neurons based on their rhythmic properties. Putative pacemaker neurons showed constitutive theta rhythmic activity and synchronized their frequencies during

hippocampal theta oscillations in different rodent theta model systems. This mechanism, known as Huygens synchronization, was reproduced by a network model of minimalistic theta-rhythmic inhibitory MS units, demonstrating that a homogeneous group of pacemakers can synchronize and desynchronize via inhibitory connections upon changing levels of tonic excitatory drive. Optogenetic tagging confirmed that pacemaker neurons are PV-expressing GABAergic cells, while non-PV GABAergic neurons likely do not participate in rhythm genesis. Glutamatergic septal neurons were of tonic theta ON type, which suggests that they contribute to the non-rhythmic excitatory control of the pacemaker rhythm generator network. In line with this prediction, optogenetic activation of MS glutamatergic neurons at 20 Hz induced theta oscillation in CA1.

We first performed an unbiased physiological characterization of MS units, extending previous electrophysiology studies (Apartis et al., 1998; Borhegyi et al., 2004; Duque et al., 2000; Ford et al., 1989; Hassani et al., 2009; Simon et al., 2006; Stewart and Fox, 1989; Varga et al., 2008). Bland and colleagues characterized MS neurons as theta-on versus theta-off based on their firing rate changes, and phasic (theta bursting) versus tonic (non-rhythmic) based on their firing patters. Petsche et al. (1962) described A- and B-units, where B-units were phase locked to theta with a stable phase relationship. Many studies have since investigated B-units (Apartis et al., 1998; Borhegyi et al., 2004; Joshi et al., 2017; King et al., 1998; Stewart and Fox, 1989), but A-units received less attention. Other studies indicated the presence of lower frequency rhythms, including "slow oscillations" and rhythmic activity related to breathing (Buzsaki et al., 1986; Tsanov, 2015; Tsanov et al., 2014; Wolansky et al., 2006). In accordance, we also observed rhythmic activity in the delta frequency band, especially in urethane-anesthetized rats. Therefore, we characterized MS neurons based on their rhythmicity during hippocampal theta and non-theta episodes as non-rhythmic, delta-rhythmic or theta-rhythmic. While this resulted in nine theoretical combinations, most MS neurons belonged to a few characteristic types.

Stewart and Fox (1989) found that, after eliminating theta oscillation in the hippocampus of urethane-anesthetized rats using atropine, a subset of MS neurons remained theta rhythmic. In another study, 15% of septal neurons were found phasic bursting even during non-theta epochs under anesthesia (Ford et al., 1989). We identified putative pacemaker neurons that fired theta-rhythmic bursts regardless of whether theta oscillation was present in CA1. This group comprised 13% of MS neurons in freely moving mice; however, we found a lower percentage of rhythmic bursting neurons in anesthetized rodents, in line with some previous reports (King et al., 1998; Stewart and Fox, 1989). The differences in percentage of pacemakers across reports may stem both from biased sampling, as the MS can be identified during recording based on the presence of theta-rhythmic activity, as well as from strictness of definitions for rhythmicity. We applied relatively conservative inclusion criteria for significant rhythmicity (Figure S2) to ensure data quality necessary for analyzing mechanisms of rhythmic synchronization, which may have resulted in a lower percentage of putative pacemakers in our datasets. These results also suggest that some MS neurons may be identified as putative pacemakers under awake but not in anesthetized conditions.

The expression of PV and HCN, the channel protein that underlies the H-current, has been associated with rhythmic pacemaking properties of MS GABAergic neurons (Borhegyi et al., 2004; Kocsis and Li, 2004; Varga et al., 2008; Xu et al., 2004). However, other studies suggested that rhythmic MS glutamatergic or cholinergic neurons may act as pacemakers (Manseau et al., 2005; Mysin et al., 2015; Smythe et al., 1992; Ujfalussy and Kiss, 2006; but see Vandecasteele et al., 2014). Here, we confirmed by optogenetic identification of multiple MS cell types that PV-expressing GABAergic neurons probably constitute most of the constitutive theta-rhythmic group. At the same time, we found that GABAergic neurons as a population contained only few theta-rhythmic neurons, suggesting that their subset that were rhythmic may have been PV expressing. We confirmed that septal pacemakers formed two groups with opposing phase preference with respect to the hippocampal theta oscillation in urethane-anesthetized rats, as reported previously (Borhegyi et al., 2004; Joshi et al., 2017; Varga et al., 2008).

We referred to MS neurons only showing theta-rhythmic bursting when hippocampal theta was present as follower neurons; their firing patterns tended to correspond with hippocampal network states. However, this property does not exclude them from participating in theta genesis. Indeed, these neurons tended to strongly synchronize with each other and putative pacemaker neurons both during theta and non-theta states, and optogenetic tagging experiments revealed an enrichment of both putative pacemaker and follower neurons in the PV+ GABAergic group (Figure S15J), suggesting that this functional distinction based on rhythmicity may occur within the anatomically defined PV-expressing group.

In the seventeenth century, Christiaan Huygens observed that two pendulum clocks, coupled through a house beam, tended to synchronize over time, which he referred to as "sympathy of two clocks" (Huygens, 1673; Oliveira and Melo, 2015; Ramirez et al., 2016; Willms et al., 2017). Such synchronization of coupled oscillators, where individual oscillators become closer to each other in their frequency and period time, has been found in many dynamical systems (Equihua and Ramirez, 2018; Ramirez et al., 2016). We identified this mechanism among MS pacemaker neurons, suggesting that a Huygens synchronization mechanism underlies the generation of a strong theta rhythmic output transmitted to the hippocampus. The two dominant oscillatory behaviors that emerge in coupled oscillators during Huygens synchronization are in-phase and anti-phase synchronization (Korteweg, 1906; Ramirez et al., 2014), and either one can sufficiently underlie frequency synchronization (Czolczynski et al., 2011; Ramirez et al., 2014, 2016). This may, at least in part, explain the observation of anti-phase firing in the MS of urethane-anesthetized rats. Experiments and modeling studies also observed less common modes of Huygens synchronization, including partial synchronization, when oscillators synchronize with a phase difference of less than 180°; "quenching," when the two oscillators suppress each other; "beating death," in which one oscillator is suppressed but remains oscillatory owing to the influence of the other; and amplitude modulation, a consequence of mutual influence (Ramirez et al., 2014). It will be

exciting to study whether and how the broad theory behind Huygens synchronization, often investigating limit behavior of complex non-linear ordinary differential equation systems, can be applied to neural circuits. For instance, "modulating" behavior can theoretically be related to forms of cross-frequency coupling (Buzsáki and Wang, 2012; Lisman and Jensen, 2013), whereas quenching and beating death can be viewed as synchronization failures, which may be relevant to oscillopathies, e.g. gamma oscillation failures in patients with schizophrenia (Hunt et al., 2017). Theoretical studies may explain how and why the output oscillation period may differ from the eigenperiods of the coupled individual oscillators (Dilão, 2009; Ramirez et al., 2016), also observed in the context of neuronal oscillations, possibly serving as a basis for phase precession (Geisler et al., 2007; O'Keefe and Recce, 1993; Zutshi et al., 2018).

Previous models of the septal pacemaker network either explored GABAergic (Denham and Borisyuk, 2000; Ujfalussy and Kiss, 2006; Wang, 2002) or glutamatergic (Ujfalussy and Kiss, 2006) pacing mechanisms. These previous works already contained indirect reference to potential Huygens synchronization mechanisms. For instance, Wang suggested that desynchronized septal pacemaker units may oscillate at different frequencies (see Figure 4 in Wang, 2002). Additionally, Ujfalussy et al. wrote that "blocking the GABAergic synapses in our ping-pong model causes desynchronization of these neurons but the cells remain theta periodic." However, Huygens synchronization has neither been experimentally tested nor directly modelled, and previous models mostly focused on exploring the ways different oscillator networks may interplay, such as two GABAergic MS groups with opposing firing phase (Ujfalussy and Kiss, 2006), MS and CA1 GABAergic groups (Denham and Borisyuk, 2000; Wang, 2002; Zou et al., 2011), or MS GABAergic and glutamatergic neurons (Mysin et al., 2015). Thus, in previous ping pong models, the synchronization mechanism required the presence of at least two dedicated inhibitory groups, with biased, non-random connectivity between the groups. In contrast, we found that even a minimalistic, homogeneous network of MS GABAergic pacemakers was sufficient to generate coherent theta-rhythmic output upon increased tonic excitation. While desynchronization of the MS network was rarely addressed in previous theoretical work, we also found that our MS model network showed rapid spontaneous desynchronization when tonic excitation was decreasing. This MS model network could recapitulate multiple features of the *in vivo* synchronization process, including Huygens synchronization, increased firing rate, faster rhythmic firing, decreased theta skipping, and a slight increase in intra-burst firing frequency.

We found a substantial increase in the firing rates in MS pacemaker neurons upon theta onset. This finding is in line with previous studies suggesting that an increased tonic excitatory drive can switch the MS network into theta state (Korvasová et al., 2021; Lu et al., 2011; Müller and Remy, 2018; Oddie et al., 1996; Ujfalussy and Kiss, 2006). Multiple cell types and pathways were proposed to contribute to this excitatory drive, including MS cholinergic, glutamatergic, and ascending brainstem inputs (Hajszan et al., 2004; Leranth and Frotscher, 1989; Müller and Remy, 2018; Oddie and Bland, 1998; Zaborszky et al., 2012). We found that MS glutamatergic neurons strongly and non-rhythmically increased their firing rates at the onset of CA1 theta, suggesting they may be the dominant relay that conveys changing levels of tonic excitation to the MS pacemaker network, in agreement with anatomical findings showing that local excitatory neurons provide the majority of excitatory inputs to MS GABAergic neurons (Hajszan et al., 2004).

In line with this, the optogenetic activation of MS glutamatergic neurons induced theta oscillation in the CA1. Importantly, we evoked theta rhythm by using a stimulation frequency of 20 Hz well above the theta range, demonstrating that VGLUT2-expressing MS neurons are capable of theta induction not only when stimulated at theta-range frequencies (Robinson et al., 2016). These results are also consistent with the growing body of evidence showing that these neurons are involved in conveying locomotion-related activation to other cell types of the MS and beyond (Fuhrmann et al., 2015; Justus et al., 2017; Korvasová et al., 2021; Oddie et al., 1996; Teitelbaum et al., 1975).

Previous studies demonstrated theta-skipping behavior of rhythmic neurons both in the entorhinal cortex (EC) (Brandon et al., 2013; Jeffery et al., 1995) and in the MS (Kay et al., 2020; King et al., 1998; Varga et al., 2008). Theta skipping was characterized by rhythmic activity with one-half the frequency of ongoing hippocampal theta, by neurons firing rhythmically in every second theta cycle. It has been demonstrated that MS input was necessary for theta-skipping behavior in the EC in rats (Brandon et al., 2013), and that theta-skipping behavior in the EC may rely on inhibitory rebound mechanisms, potentially crucial to the formation of characteristic grid cell firing fields (Hasselmo, 2014). We confirmed the presence of theta-skipping neurons in the MS of urethane-anesthetized rats. While some of these neurons fired regularly in every second cycle, other neurons showed a less regular pattern, occasionally skipping more than one cycle. Interestingly, we found very few theta-skipping neurons in anesthetized and freely moving mice. Therefore, theta-skipping in the MS may not be necessary for grid pattern formation in mice.

We found a group of tonically active neurons both in rats and mice, which may be cholinergic, since (1) their firing patterns resemble cholinergic neurons in previous publications (Brazhnik and Fox, 1997; Mamad et al., 2015; Tsanov, 2015), (2) we identified cholinergic neurons with similar rhythmic and synchronization properties from other basal forebrain structures (Laszlovszky et al., 2020), and (3) rhythmic basal forebrain cholinergic neurons were not phase locked to hippocampal theta in a former study (Lee et al., 2005), as we also found for the tonically active group. Theta-rhythmic cholinergic neurons may be more linked with a neocortical theta oscillation that can be recorded from the posterior cingulate cortex (Destrade and Ott, 1982; Lee et al., 2005), and we have also reported behavior-specific synchronization of nucleus basalis cholinergic neurons with theta-band activity in the auditory cortex (Laszlovszky et al., 2020). This would confirm that the role of MS cholinergic neurons in hippocampal theta generation is mostly indirect through GABAergic neurons, controlling theta amplitude but not participating in rhythmic theta pacing (Dannenberg et al., 2015; Lee et al., 1994; Yang et al., 2014, 2017). We expect that it

will be one of the most exciting future directions to better understand how multiple theta rhythms interact dynamically in the brain, including synchronization with active sensing processes (Moore et al., 2013; Ranade et al., 2013; Semba and Komisaruk, 1984), entraining local pacemaker groups (Manseau et al., 2008) and interacting with cellular resonance properties (Zemankovics et al., 2010).

Limitations of the study

Although we demonstrated that a homogeneous group of MS inhibitory neurons may be capable of pacing hippocampal theta, this does not rule out the possibility of other contributing neuronal populations including the hippocampo-septal feedback projection (Katona et al., 2017; Manseau et al., 2008; Toth et al., 1993; Wang, 2002) and subcortical areas such as the supramammillary nucleus (Farrell et al., 2021; Pan and McNaughton, 2002; Vertes and Kocsis, 1997) and the nucleus incertus (Ma et al., 2009; Martínez-Bellver et al., 2015; Szőnyi et al., 2019). Nevertheless, recent studies demonstrated that intraseptal connections are necessary for CA1 theta oscillations to emerge (Korvasová et al., 2021) and that the nucleus incertus may not provide but rather receive theta-rhythmic signals from the MS (Trenk et al., 2022).

An alternative mechanism to frequency synchronization is phase synchronization without concurrent change in rhythmicity frequency, defined generally as changes in the phase relationship of coupled oscillators (Rosenblum et al., 1996, 2001). Such mechanisms are known to operate between synchronizing brain regions and are thought to underlie changes in the efficacy of information transfer (Fell and Axmacher, 2011). As a special case of phase synchronization, a decrease in phase difference between individual pacemaker units may lead to a larger amplitude rhythmic output. In contrast, we demonstrated a convergence of rhythmicity frequencies during synchronization. Although this change in frequencies can be accompanied by a change in relative firing phases, it is hard to interpret whether this is a necessary consequence of the frequency synchronization, or a parallel, separate phase synchronization process also takes place (Rosenblum et al., 1996).

We found a strong consistency of rhythmic MS cell types and synchronization mechanisms across urethane-anesthetized rats, urethane-anesthetized mice and feely moving mice, while we did not obtain data from freely moving rats. This argues for common mechanisms of septo-hippocampal theta-rhythmic synchronization. However, we also noted some differences. Part of them may stem from known distinctions of urethane- and atropine-sensitive theta oscillations (Kramis et al., 1975; Li et al., 2007), with different underlying mechanisms (Losonczy et al., 2010; Mikulovic et al., 2018; Nicola and Clopath, 2019; Winterer et al., 2019). Anesthetized rats showed strong hippocampal rhythmicity in the delta band during non-theta episodes, mostly absent in mice. In accordance, we found delta-rhythmic and theta-skipping MS neurons in rats but very few in mice. Tonically active neurons showed a theta-associated firing rate decrease in rats but increase in mice. While we speculated that this group might be cholinergic, the lack of optogenetic identification of cholinergic MS neurons is another limitation of this study.

Marder and colleagues observed that often the rhythmic firing activities are controlled and not the exact underlying ion channel constellations, leading to unexpected variability in channel abundance with stable oscillatory parameters (Alonso and Marder, 2019). It is possible that, similar to this principle, the theta-rhythmic activity of the septo-hippocampal system is evolutionarily conserved, with a larger variance in the exact implementation (Payne et al., 2021). Further experiments and modeling will help gauge the significance of this variability.

STAR★METHODS

Detailed methods are provided in the online version of this paper and include the following:

- KEY RESOURCES TABLE
- RESOURCE AVAILABILITY
  - Lead contact
  - Materials availability
  - Data and code availability
- EXPERIMENTAL MODEL AND SUBJECT DETAILS
- METHOD DETAILS
  - Surgery and electrophysiological recordings
  - Histological verification of the recording location
  - Immunostaining
- QUANTIFICATION AND STATISTICAL ANALYSIS
  - Hippocampal state detection
  - Spike sorting of septal neurons
  - Rhythmicity indices of MS neurons
  - Theta-burst index
  - Analysis of phase-coupling
  - Crosscorrelation
  - Pacemaker synchronization
  - Wavelet coherence
  - Data analysis of the optogenetic tagging experiments
  - Analysis of photostimulation impact
  - MS pacemaker neuron model
  - Modeling the MS pacemaker network
  - Exploring the parameter space of the pacemaker network model
  - Model network synchronization
  - Statistical testing

SUPPLEMENTAL INFORMATION

Supplemental information can be found online at https://doi.org/10.1016/j.celrep.2022.111149.

ACKNOWLEDGMENTS

The authors thank Katalin Lengyel for technical assistance and Drs. Tim Viney and Peter Somogyi for helpful comments on the manuscript. This work was supported by the "Lendület" Program of the Hungarian Academy of Sciences (LP2015-2/2015), NKFIH KH125294, NKFIH K135561, the ERC Starting Grant no. 715043 and SPIRITS 2020 of Kyoto University to B.H.; the NRDI Office of Hungary within the framework of the Artificial Intelligence National Laboratory Program (RRF-2.3.1-21-2022-00004) to B.H., V.V., and S.K.; NKFIH K119650 to P.B.; National Brain Research Program 1.2.1-NKP-2017-00002 to P.B., R.F., and I.U.; NKFIH PD124175 and PD134196 to R.F.; NKFIH TUDFO/51757-1/2019-ITM, ELKH KEP-4/5/2021, and ELKH KÖ-39/2021 to I.U.; the

ÚNKP-20-3 New National Excellence Program of the Ministry for Innovation and Technology to B.K.; and the Generalitat Valenciana Postdoctoral Fellowship Program (APOSTD/2019/003) to S.M.B. We acknowledge the help of the Nikon Center of Excellence at the Institute of Experimental Medicine (IEM), Nikon Europe, Nikon Austria, and Auro-Science Consulting for kindly providing microscopy support and the supportive help of the Central Virus Laboratory of IEM. We thank Luigi Petrucco for open access science art at SciDraw (https://doi.org/10.5281/zenodo.3925903).

AUTHOR CONTRIBUTIONS

B.H. developed the idea and conceptualized the manuscript. S.M.B., R.F., A.D., B.H., and P.B. performed the experiments, supervised by T.F.F., I.U., V.V., and B.H. B.K., S.M.B., and P.B. performed the data analysis. B.K., K.S., and D.S. generated the figures. D.S. performed immunocytochemistry. B.K. performed the modeling, supervised by S.K. B.H. wrote the manuscript with input from all authors.

DECLARATION OF INTERESTS

The authors declare no competing financial interests.

Received: January 22, 2021
Revised: May 6, 2022
Accepted: July 7, 2022
Published: August 2, 2022

REFERENCES

Adler, A., Zhao, R., Shin, M.E., Yasuda, R., and Gan, W.-B. (2019). Somatostatin-expressing interneurons enable and maintain learning-dependent sequential activation of pyramidal neurons. Neuron *102*, 202–216.e7.

Akaike, H. (1973). Information theory and an extension of the maximum likelihood principle. In 2nd International Symposium on Information Theory, pp. 267–281.

Alonso, L.M., and Marder, E. (2019). Visualization of currents in neural models with similar behavior and different conductance densities. Elife *8*, e42722.

Apartis, E., Poindessous-Jazat, F.R., Lamour, Y.A., and Bassant, M.H. (1998). Loss of rhythmically bursting neurons in rat medial septum following selective lesion of septohippocampal cholinergic system. J. Neurophysiol. *79*, 1633–1642.

Bakker, R., Tiesinga, P., and Kötter, R. (2015). The scalable brain atlas: instant web-based access to public brain atlases and related content. Neuroinformatics *13*, 353–366.

Barthó, P., Hirase, H., Monconduit, L., Zugaro, M., Harris, K.D., and Buzsáki, G. (2004). Characterization of neocortical principal cells and interneurons by network interactions and extracellular features. J. Neurophysiol. *92*, 600–608.

Bland, B.H., Trepel, C., Oddie, S.D., and Kirk, I.J. (1996). Intraseptal microinfusion of muscimol: effects on hippocampal formation theta field activity and phasic Theta-ON cell discharges. Exp. Neurol. *138*, 286–297.

Borg-Graham, L.J. (1999). Models of cortical circuits. In Interpretations of Data and Mechanisms for Hippocampal Pyramidal Cell Models (Springer), pp. 19–138.

Borhegyi, Z., Varga, V., Szilágyi, N., Fabo, D., and Freund, T.F. (2004). Phase segregation of medial septal GABAergic neurons during hippocampal theta activity. J. Neurosci. *24*, 8470–8479.

Brandon, M.P., Bogaard, A.R., Schultheiss, N.W., and Hasselmo, M.E. (2013). Segregation of cortical head direction cell assemblies on alternating theta cycles. Nat. Neurosci. *16*, 739–748.

Brazhnik, E.S., and Fox, S.E. (1997). Intracellular recordings from medial septal neurons during hippocampal theta rhythm. Exp. Brain Res. *114*, 442–453.

Brewer, M.J., Butler, A., and Cooksley, S.L. (2016). The relative performance of AIC, AIC C and BIC in the presence of unobserved heterogeneity. Methods Ecol. Evol. *7*, 679–692.

Buzsáki, G., Czopf, J., Kondákor, I., and Kellényi, L. (1986). Laminar distribution of hippocampal rhythmic slow activity (RSA) in the behaving rat: current-source density analysis, effects of urethane and atropine. Brain Res. *365*, 125–137.

Buzsáki, G. (2002). Theta oscillations in the hippocampus. Neuron *33*, 325–340.

Buzsáki, G. (2006). Rhythms of the Brain (Oxford University Press).

Buzsáki, G., and Mizuseki, K. (2014). The log-dynamic brain: how skewed distributions affect network operations. Nat. Rev. Neurosci. *15*, 264–278.

Buzsáki, G., and Moser, E.I. (2013). Memory, navigation and theta rhythm in the hippocampal-entorhinal system. Nat. Neurosci. *16*, 130–138.

Buzsáki, G., and Wang, X.-J. (2012). Mechanisms of gamma oscillations. Annu. Rev. Neurosci. *35*, 203–225.

Carnevale, N.T., and Hines, M.L. (2006). The NEURON Book (Cambridge University Press).

Cummings, K.A., and Clem, R.L. (2020). Prefrontal somatostatin interneurons encode fear memory. Nat. Neurosci. *23*, 61–74.

Cutsuridis, V., and Poirazi, P. (2015). A computational study on how theta modulated inhibition can account for the long temporal windows in the entorhinal-hippocampal loop. Neurobiol. Learn. Mem. *120*, 69–83.

Czolczynski, K., Perlikowski, P., Stefanski, A., and Kapitaniak, T. (2011). Huygens' odd sympathy experiment revisited. Int. J. Bifurcation Chaos *21*, 2047–2056.

Dannenberg, H., Pabst, M., Braganza, O., Schoch, S., Niediek, J., Bayraktar, M., Mormann, F., and Beck, H. (2015). Synergy of direct and indirect cholinergic septo-hippocampal pathways coordinates firing in hippocampal networks. J. Neurosci. *35*, 8394–8410.

Denham, M.J., and Borisyuk, R.M. (2000). A model of theta rhythm production in the septal-hippocampal system and its modulation by ascending brain stem pathways. Hippocampus *10*, 698–716.

Destrade, C., and Ott, T. (1982). Is a retrosplenial (cingulate) pathway involved in the mediation of high frequency hippocampal rhythmical slow activity (theta)? Brain Res. *252*, 29–37.

DiCarlo, J.J., Lane, J.W., Hsiao, S.S., and Johnson, K.O. (1996). Marking microelectrode penetrations with fluorescent dyes. J. Neurosci. Methods *64*, 75–81.

Dilão, R. (2009). Antiphase and in-phase synchronization of nonlinear oscillators: the Huygens's clocks system. Chaos *19*, 023118.

Duque, A., Balatoni, B., Detari, L., and Zaborszky, L. (2000). EEG correlation of the discharge properties of identified neurons in the basal forebrain. J. Neurophysiol. *84*, 1627–1635.

Equihua, G.G.V., and Ramirez, J.P. (2018). Synchronization of hindmarsh-rose synchronization of hindmarsh-rose synchronization of hindmarsh-rose neurons huygens-like coupling synchronization of hindmarsh-rose neurons huygens-like coupling huygens-like coupling. IFAC-PapersOnLine *51*, 186–191.

Farrell, J.S., Lovett-Barron, M., Klein, P.M., Sparks, F.T., Gschwind, T., Ortiz, A.L., Ahanonu, B., Bradbury, S., Terada, S., Oijala, M., et al. (2021). Supramammillary regulation of locomotion and hippocampal activity. Science *374*, 1492–1496.

Fell, J., and Axmacher, N. (2011). The role of phase synchronization in memory processes. Nat. Rev. Neurosci. *12*, 105–118.

Fiáth, R., Raducanu, B.C., Musa, S., Andrei, A., Lopez, C.M., van Hoof, C., Ruther, P., Aarts, A., Horváth, D., and Ulbert, I. (2018). A silicon-based neural probe with densely-packed low-impedance titanium nitride microelectrodes for ultrahigh-resolution in vivo recordings. Biosens. Bioelectron. *106*, 86–92.

Fiáth, R., Márton, A.L., Mátyás, F., Pinke, D., Márton, G., Tóth, K., and Ulbert, I. (2019). Slow insertion of silicon probes improves the quality of acute neuronal recordings. Sci. Rep. *9*, 111.

Fisher, N.I. (1993). Statistical Analysis of Circular Data (Cambridge University Press).

Ford, R.D., Colom, L.V., and Bland, B.H. (1989). The classification of medial septum-diagonal band cells as σ-on or σ-off in relation to hippocampal EEG states. Brain Res. *493*, 269–282.

Freund, T.F. (1989). GABAergic septohippocampal neurons contain parvalbumin. Brain Res. *478*, 375–381.

Freund, T.F., and Antal, M. (1988). GABA-containing neurons in the septum control inhibitory interneurons in the hippocampus. Nature *336*, 170–173.

Fuhrmann, F., Justus, D., Sosulina, L., Kaneko, H., Beutel, T., Friedrichs, D., Schoch, S., Schwarz, M.K., Fuhrmann, M., and Remy, S. (2015). Locomotion, theta oscillations, and the speed-correlated firing of hippocampal neurons are controlled by a medial septal glutamatergic circuit. Neuron *86*, 1253–1264.

Geisler, C., Robbe, D., Zugaro, M., Sirota, A., and Buzsáki, G. (2007). Hippocampal place cell assemblies are speed-controlled oscillators. Proc. Natl. Acad. Sci. USA *104*, 8149–8154.

Golomb, D., Donner, K., Shacham, L., Shlosberg, D., Amitai, Y., and Hansel, D. (2007). Mechanisms of firing patterns in fast-spiking cortical interneurons. PLoS Comput. Biol. *3*, e156.

Green, J.D., and Arduini, A.A. (1954). Hippocampal electrical activity in arousal. J. Neurophysiol. *17*, 533–557.

Green, J.D., Maxwell, D.S., Schindler, W.J., and Stumpf, C. (1960). Rabbit eeg "theta" rhythm: its anatomical source and relation to activity in single neurons. J. Neurophysiol. *23*, 403–420.

Gritti, I., Manns, I.D., Mainville, L., and Jones, B.E. (2003). Parvalbumin, calbindin, or calretinin in cortically projecting and GABAergic, cholinergic, or glutamatergic basal forebrain neurons of the rat. J. Comp. Neurol. *458*, 11–31.

Gritti, I., Henny, P., Galloni, F., Mainville, L., Mariotti, M., and Jones, B.E. (2006). Stereological estimates of the basal forebrain cell population in the rat, including neurons containing choline acetyltransferase, glutamic acid decarboxylase or phosphate-activated glutaminase and colocalizing vesicular glutamate transporters. Neuroscience *143*, 1051–1064.

Hajszan, T., Alreja, M., and Leranth, C. (2004). Intrinsic vesicular glutamate transporter 2-immunoreactive input to septohippocampal parvalbumin-containing neurons: novel glutamatergic local circuit cells. Hippocampus *14*, 499–509.

Hangya, B., Borhegyi, Z., Szilágyi, N., Freund, T.F., and Varga, V. (2009). GABAergic neurons of the medial septum lead the hippocampal network during theta activity. J. Neurosci. *29*, 8094–8102.

Hassani, O.K., Lee, M.G., Henny, P., and Jones, B.E. (2009). Discharge profiles of identified GABAergic in comparison to cholinergic and putative glutamatergic basal forebrain neurons across the sleep-wake cycle. J. Neurosci. *29*, 11828–11840.

Hasselmo, M.E. (2014). Neuronal rebound spiking, resonance frequency and theta cycle skipping may contribute to grid cell firing in medial entorhinal cortex. Philos. Trans. R. Soc. Lond. B Biol. Sci. *369*, 20120523.

Hunt, M.J., Kopell, N.J., Traub, R.D., and Whittington, M.A. (2017). Aberrant network activity in schizophrenia. Trends Neurosci. *40*, 371–382.

Huygens, C. (1673). Horologium Oscillatorium: sive de motu pendulorum ad horologia aptato demonstrationes geometricae (F. Muguet).

Inokawa, H., Yamada, H., Matsumoto, N., Muranishi, M., and Kimura, M. (2010). Juxtacellular labeling of tonically active neurons and phasically active neurons in the rat striatum. Neuroscience *168*, 395–404.

Jeffery, K.J., Donnett, J.G., and O'Keefe, J. (1995). Medial septal control of theta-correlated unit firing in the entorhinal cortex of awake rats. Neuroreport *6*, 2166–2170.

Joshi, A., Salib, M., Viney, T.J., Dupret, D., and Somogyi, P. (2017). Behavior-dependent activity and synaptic organization of septo-hippocampal GABAergic neurons selectively targeting the hippocampal CA3 area. Neuron *96*, 1342–1357.e5.

Justus, D., Dalügge, D., Bothe, S., Fuhrmann, F., Hannes, C., Kaneko, H., Friedrichs, D., Sosulina, L., Schwarz, I., Elliott, D.A., et al. (2017). Glutamatergic synaptic integration of locomotion speed via septoentorhinal projections. Nat. Neurosci. *20*, 16–19.

Kahana, M.J., Sekuler, R., Caplan, J.B., Kirschen, M., and Madsen, J.R. (1999). Human theta oscillations exhibit task dependence during virtual maze navigation. Nature *399*, 781–784.

Káli, S., and Zemankovics, R. (2012). The effect of dendritic voltage-gated conductances on the neuronal impedance: a quantitative model. J. Comput. Neurosci. *33*, 257–284.

Katona, L., Micklem, B., Borhegyi, Z., Swiejkowski, D.A., Valenti, O., Viney, T.J., Kotzadimitriou, D., Klausberger, T., and Somogyi, P. (2017). Behavior-dependent activity patterns of GABAergic long-range projecting neurons in the rat hippocampus. Hippocampus *27*, 359–377.

Kay, K., Chung, J.E., Sosa, M., Schor, J.S., Karlsson, M.P., Larkin, M.C., Liu, D.F., and Frank, L.M. (2020). Constant sub-second cycling between representations of possible futures in the Hippocampus. Cell *180*, 552–567.e25.

Kim, T., Thankachan, S., McKenna, J.T., McNally, J.M., Yang, C., Choi, J.H., Chen, L., Kocsis, B., Deisseroth, K., Strecker, R.E., et al. (2015). Cortically projecting basal forebrain parvalbumin neurons regulate cortical gamma band oscillations. Proc. Natl. Acad. Sci. USA *112*, 3535–3540.

King, C., Recce, M., and O'Keefe, J. (1998). The rhythmicity of cells of the medial septum/diagonal band of Broca in the awake freely moving rat: relationships with behaviour and hippocampal theta. Eur. J. Neurosci. *10*, 464–477.

Kiss, J., Patel, A.J., Baimbridge, K.G., and Freund, T.F. (1990). Topographical localization of neurons containing parvalbumin and choline acetyltransferase in the medial septum-diagonal band region of the rat. Neuroscience *36*, 61–72.

Klausberger, T., and Somogyi, P. (2008). Neuronal diversity and temporal dynamics: the unity of hippocampal circuit operations. Science *321*, 53–57.

Kocsis, B., and Li, S. (2004). In vivo contribution of h-channels in the septal pacemaker to theta rhythm generation. Eur. J. Neurosci. *20*, 2149–2158.

Konishi, S., and Kitagawa, G. (2008). Information Criteria and Statistical Modeling (Springer).

Korteweg, D. (1906). Les horloges sympathiques de Huygens. Arch. Neerl. Des Sci. Exactes Nat. *11*, 273–296.

Korvasová, K., Ludwig, F., Kaneko, H., Sosulina, L., Tetzlaff, T., Remy, S., and Mikulovic, S. (2021). Locomotion induced by medial septal glutamatergic neurons is linked to intrinsically generated persistent ring. Preprint at bioRxiv. https://doi.org/10.1101/2021.04.23.441122.

Kramis, R., Vanderwolf, C.H., and Bland, B.H. (1975). Two types of hippocampal rhythmical slow activity in both the rabbit and the rat: relations to behavior and effects of atropine, diethyl ether, urethane, and pentobarbital. Exp. Neurol. *49*, 58–85.

Kvitsiani, D., Ranade, S., Hangya, B., Taniguchi, H., Huang, J.Z., and Kepecs, A. (2013). Distinct behavioural and network correlates of two interneuron types in prefrontal cortex. Nature *498*, 363–366.

Laszlovszky, T., Schlingloff, D., Hegedüs, P., Freund, T.F., Gulyás, A., Kepecs, A., and Hangya, B. (2020). Distinct synchronization, cortical coupling and behavioral function of two basal forebrain cholinergic neuron types. Nat. Neurosci. *23*, 992–1003.

Lee, M.G., Chrobak, J.J., Sik, A., Wiley, R.G., and Buzsáki, G. (1994). Hippocampal theta activity following selective lesion of the septal cholinergic system. Neuroscience *62*, 1033–1047.

Lee, M.G., Hassani, O.K., Alonso, A., and Jones, B.E. (2005). Cholinergic basal forebrain neurons burst with theta during waking and paradoxical sleep. J. Neurosci. *25*, 4365–4369.

Leranth, C., and Frotscher, M. (1989). Organization of the septal region in the rat brain: cholinergic-GABAergic interconnections and the termination of hippocampo-septal fibers. J. Comp. Neurol. *289*, 304–314.

Li, S., Topchiy, I., and Kocsis, B. (2007). The effect of atropine administered in the medial septum or hippocampus on high- and low-frequency theta rhythms in the hippocampus of urethane anesthetized rats. Synapse *61*, 412–419.

Lima, S.Q., Hromádka, T., Znamenskiy, P., and Zador, A.M. (2009). PINP: a new method of tagging neuronal populations for identification during in vivo electrophysiological recording. PLoS One *4*, e6099.

Lisman, J.E., and Jensen, O. (2013). The theta-gamma neural code. Neuron *77*, 1002–1016.

Losonczy, A., Zemelman, B.V., Vaziri, A., and Magee, J.C. (2010). Network mechanisms of theta related neuronal activity in hippocampal CA1 pyramidal neurons. Nat. Neurosci. *13*, 967–972.

Lu, C.B., Ouyang, G., Henderson, Z., and Li, X. (2011). Induction of theta-frequency oscillations in the rat medial septal diagonal band slice by metabotropic glutamate receptor agonists. Neuroscience *177*, 1–11.

Ma, S., Olucha-Bordonau, F.E., Hossain, M.A., Lin, F., Kuei, C., Liu, C., Wade, J.D., Sutton, S.W., Nuñez, A., and Gundlach, A.L. (2009). Modulation of hippocampal theta oscillations and spatial memory by relaxin-3 neurons of the nucleus incertus. Learn. Mem. *16*, 730–742.

Mamad, O., McNamara, H.M., Reilly, R.B., and Tsanov, M. (2015). Medial septum regulates the hippocampal spatial representation. Front. Behav. Neurosci. *9*, 166–216.

Manseau, F., Danik, M., and Williams, S. (2005). A functional glutamatergic neurone network in the medial septum and diagonal band area. J. Physiol. *566*, 865–884.

Manseau, F., Goutagny, R., Danik, M., and Williams, S. (2008). The hippocamposeptal pathway generates rhythmic firing of GABAergic neurons in the medial septum and diagonal bands: an investigation using a complete septohippocampal preparation in vitro. J. Neurosci. *28*, 4096–4107.

Martínez-Bellver, S., Cervera-Ferri, A., Martínez-Ricós, J., Ruiz-Torner, A., Luque-García, A., Luque-Martinez, A., Blasco-Serra, A., Guerrero-Martínez, J., Bataller-Mompeán, M., and Teruel-Martí, V. (2015). Regular theta-firing neurons in the nucleus incertus during sustained hippocampal activation. Eur. J. Neurosci. *41*, 1049–1067.

McNamara, C.G., Tejero-Cantero, Á., Trouche, S., Campo-Urriza, N., and Dupret, D. (2014). Dopaminergic neurons promote hippocampal reactivation and spatial memory persistence. Nat. Neurosci. *17*, 1658–1660.

Migliore, M., and Migliore, R. (2012). Know your current I(h): interaction with a shunting current explains the puzzling effects of its pharmacological or pathological modulations. PLoS One *7*, e36867.

Mikulovic, S., Restrepo, C.E., Siwani, S., Bauer, P., Pupe, S., Tort, A.B.L., Kullander, K., and Leão, R.N. (2018). Ventral hippocampal OLM cells control type 2 theta oscillations and response to predator odor. Nat. Commun. *9*, 3638.

Moldestad, O., Karlsen, P., Molden, S., and Storm, J.F. (2009). Tracheotomy improves experiment success rate in mice during urethane anesthesia and stereotaxic surgery. J. Neurosci. Methods *176*, 57–62.

Moore, J.D., Deschênes, M., Furuta, T., Huber, D., Smear, M.C., Demers, M., and Kleinfeld, D. (2013). Hierarchy of orofacial rhythms revealed through whisking and breathing. Nature *497*, 205–210.

Morris, N.P., Fyffe, R.E.W., and Robertson, B. (2004). Characterisation of hyperpolarization-activated currents (Ih) in the medial septum/diagonal band complex in the mouse. Brain Res. *1006*, 74–86.

Müller, C., and Remy, S. (2018). Septo–hippocampal interaction. Cell Tissue Res. *373*, 565–575.

Mysin, I.E., Kitchigina, V.F., and Kazanovich, Y. (2015). Modeling synchronous theta activity in the medial septum: key role of local communications between different cell populations. J. Comput. Neurosci. *39*, 1–16.

Nicola, W., and Clopath, C. (2019). A diversity of interneurons and Hebbian plasticity facilitate rapid compressible learning in the hippocampus. Nat. Neurosci. *22*, 1168–1181.

O'Keefe, J., and Recce, M.L. (1993). Phase Relationship between Hippocampal Place Units and the EEG Theta Rhythm. Hippocampus *3*, 317–330.

Oddie, S.D., and Bland, B.H. (1998). Hippocampal formation theta activity and movement selection. Neurosci. Biobehav. Rev. *22*, 221–231.

Oddie, S.D., Stefanek, W., Kirk, I.J., and Bland, B.H. (1996). Intraseptal procaine abolishes hypothalamic stimulation-induced wheel-running and hippocampal theta field activity in rats. J. Neurosci. *16*, 1948–1956.

Oliveira, H.M., and Melo, L.V. (2015). Huygens synchronization of two clocks. Sci. Rep. *5*, 11548–11612.

Pachitariu, M., Steinmetz, N., Kadir, S., Carandini, M., and Harris, K.D. (2016). Kilosort: realtime spike-sorting for extracellular electrophysiology with hundreds of channels. Preprint at bioRxiv. https://doi.org/10.1101/061481.

Pan, W.-X., and McNaughton, N. (2002). The role of the medial supramammillary nucleus in the control of hippocampal theta activity and behaviour in rats. Eur. J. Neurosci. *16*, 1797–1809.

Paxinos, G., Franklin, K.B.J., and Franklin, K.B.J. (2001). The Mouse Brain in Stereotaxic Coordinates (Academic Press).

Payne, H.L., Lynch, G.F., and Aronov, D. (2021). Neural representations of space in the hippocampus of a food-caching bird. Science *373*, 343–348.

Petsche, H., Stumpf, C., and Gogolak, G. (1962). The significance of the rabbit's septum as a relay station between the midbrain and the hippocampus I. The control of hippocampus arousal activity by the septum cells. Electroencephalogr. Clin. Neurophysiol. *14*, 202–211.

Peña Ramirez, J., Fey, R.H.B., Aihara, K., and Nijmeijer, H. (2014). An improved model for the classical Huygens ' experiment on synchronization of pendulum clocks. J. Sound Vib. *333*, 7248–7266.

Ramirez, J.P., Olvera, L.A., Nijmeijer, H., and Alvarez, J. (2016). The sympathy of two pendulum clocks: beyond Huygens' observations. Sci. Rep. *6*, 1–16.

Ranade, S., Hangya, B., and Kepecs, A. (2013). Multiple modes of phase locking between sniffing and whisking during active exploration. J. Neurosci. *33*, 8250–8256.

Robinson, J., Manseau, F., Ducharme, G., Amilhon, B., Vigneault, E., El Mestikawy, S., and Williams, S. (2016). Optogenetic activation of septal glutamatergic neurons drive hippocampal theta rhythms. J. Neurosci. *36*, 3016–3023.

Rosenblum, M., Pikovsky, A., Kurths, J., Schäfer, C., and Tass, P.A. (2001). Phase synchronization: from theory to data analysis. Handb. Biol. Phys. *4*, 279–321.

Rosenblum, M.G., Pikovsky, A.S., and Kurths, J. (1996). Phase synchronization of chaotic oscillators. Phys. Rev. Lett. *76*, 1804–1807.

Rossant, C., Kadir, S.N., Goodman, D.F.M., Schulman, J., Hunter, M.L.D., Saleem, A.B., Grosmark, A., Belluscio, M., Denfield, G.H., Ecker, A.S., et al. (2016). Spike sorting for large, dense electrode arrays. Nat. Neurosci. *19*, 634–641.

Rutishauser, U., Ross, I.B., Mamelak, A.N., and Schuman, E.M. (2010). Human memory strength is predicted by theta-frequency phase-locking of single neurons. Nature *464*, 903–907.

Semba, K., and Komisaruk, B.R. (1984). Neural substrates of two different rhythmical vibrissal movements in the rat. Neuroscience *12*, 761–774.

Simon, A.P., Poindessous-Jazat, F., Dutar, P., Epelbaum, J., and Bassant, M.H. (2006). Firing properties of anatomically identified neurons in the medial septum of anesthetized and unanesthetized restrained rats. J. Neurosci. *26*, 9038–9046.

Smythe, J.W., Colom, L.V., and Bland, B.H. (1992). The extrinsic modulation of hippocampal theta depends on the coactivation of cholinergic and GABA-ergic medial septal inputs. Neurosci. Biobehav. Rev. *16*, 289–308.

Sotty, F., Danik, M., Manseau, F., Laplante, F., Quirion, R., and Williams, S. (2003). Distinct electrophysiological properties of glutamatergic, cholinergic and GABAergic rat septohippocampal neurons: novel implications for hippocampal rhythmicity. J. Physiol. *551*, 927–943.

Stewart, M., and Fox, S.E. (1989). Two populations of rhythmically bursting neurons in rat medial septum are revealed by atropine. J. Neurophysiol. *61*, 982–993.

Széll, A., Martínez-Bellver, S., Hegedüs, P., and Hangya, B. (2020). OPETH: open source solution for real-time peri-event time histogram based on open Ephys. Front. Neuroinf. *14*, 21.

Szőnyi, A., Sos, K.E., Nyilas, R., Schlingloff, D., Domonkos, A., Takács, V.T., Pósfai, B., Hegedüs, P., Priestley, J.B., Gundlach, A.L., et al. (2019). Brainstem nucleus incertus controls contextual memory formation. Science *364*, eaaw0445.

Teitelbaum, H., Lee, J.F., and Johannessen, J.N. (1975). Behaviorally evoked hippocampal theta waves: a cholinergic response. Science *188*, 1114–1116.

Tokuda, K., Katori, Y., and Aihara, K. (2019). Chaotic dynamics as a mechanism of rapid transition of hippocampal local field activity between theta and non-theta states. Chaos *29*, 113115.

Tóth, K., Borhegyi, Z., and Freund, T.F. (1993). Postsynaptic targets of GABAergic hippocampal neurons in the medial septum-diagonal band of Broca complex. J. Neurosci. *13*, 3712–3724.

Trenk, A., Walczak, M., Szlaga, A., Pradel, K., Blasiak, A., and Blasiak, T. (2022). Bidirectional communication between the pontine nucleus incertus and the medial septum is carried out by electrophysiologically-distinct neuronal populations. J. Neurosci. *42*, 2234–2252.

Tsanov, M. (2015). Septo-hippocampal signal processing: breaking the code. Prog. Brain Res. *219*, 103–120.

Tsanov, M., Chah, E., Reilly, R., and O'Mara, S.M. (2014). Respiratory cycle entrainment of septal neurons mediates the fast coupling of sniffing rate and hippocampal theta rhythm. Eur. J. Neurosci. *39*, 957–974.

Ujfalussy, B., and Kiss, T. (2006). How do glutamatergic and GABAergic cells contribute to synchronization in the medial septum? J. Comput. Neurosci. *21*, 343–357.

Umbriaco, D., Watkins, K.C., Descarries, L., Cozzari, C., and Hartman, B.K. (1994). Ultrastructural and morphometric features of the acetylcholine innervation in adult rat parietal cortex: an electron microscopic study in serial sections. J. Comp. Neurol. *348*, 351–373.

Unal, G., Joshi, A., Viney, T.J., Kis, V., and Somogyi, P. (2015). Synaptic targets of medial septal projections in the Hippocampus and extrahippocampal cortices of the mouse. J. Neurosci. *35*, 15812–15826.

Vandecasteele, M., Varga, V., Berényi, A., Papp, E., Barthó, P., Venance, L., Freund, T.F., and Buzsáki, G. (2014). Optogenetic activation of septal cholinergic neurons suppresses sharp wave ripples and enhances theta oscillations in the hippocampus. Proc. Natl. Acad. Sci. USA *111*, 13535–13540.

Varga, V., Hangya, B., Kránitz, K., Ludányi, A., Zemankovics, R., Katona, I., Shigemoto, R., Freund, T.F., and Borhegyi, Z. (2008). The presence of pacemaker HCN channels identifies theta rhythmic GABAergic neurons in the medial septum. J. Physiol. *586*, 3893–3915.

Vertes, R.P., and Kocsis, B. (1997). Brainstem-diencephalo-septohippocampal systems controlling the theta rhythm of the hippocampus. Neuroscience *81*, 893–926.

Viney, T.J., Salib, M., Joshi, A., Unal, G., Berry, N., and Somogyi, P. (2018). Shared rhythmic subcortical GABAergic input to the entorhinal cortex and presubiculum. Elife *7*, 1–35.

Wang, X.-J. (2002). Pacemaker neurons for the theta rhythm and their synchronization in the septohippocampal reciprocal loop. J. Neurophysiol. *87*, 889–900.

Wikenheiser, A.M., and Redish, A.D. (2013). The balance of forward and backward hippocampal sequences shifts across behavioral states. Hippocampus *23*, 22–29.

Willms, A.R., Kitanov, P.M., and Langford, W.F. (2017). Huygens' clocks revisited. R. Soc. Open Sci. *4*, 170777.

Winterer, J., Lukacsovich, D., Que, L., Sartori, A.M., Luo, W., and Földy, C. (2019). Single-cell RNA-Seq characterization of anatomically identified OLM interneurons in different transgenic mouse lines. Eur. J. Neurosci. *50*, 3750–3771.

Wolansky, T., Clement, E.A., Peters, S.R., Palczak, M.A., and Dickson, C.T. (2006). Hippocampal slow oscillation: a novel EEG state and its coordination with ongoing neocortical activity. J. Neurosci. *26*, 6213–6229.

Xu, C., Datta, S., Wu, M., and Alreja, M. (2004). Hippocampal theta rhythm is reduced by suppression of the H-current in septohippocampal GABAergic neurons. Eur. J. Neurosci. *19*, 2299–2309.

Yang, C., McKenna, J.T., Zant, J.C., Winston, S., Basheer, R., and Brown, R.E. (2014). Cholinergic neurons excite cortically projecting basal forebrain GABAergic neurons. J. Neurosci. *34*, 2832–2844.

Yang, C., Thankachan, S., McCarley, R.W., and Brown, R.E. (2017). The menagerie of the basal forebrain: how many (neural) species are there, what do they look like, how do they behave and who talks to whom? Curr. Opin. Neurobiol. *44*, 159–166.

Yoder, R.M., and Pang, K.C.H. (2005). Involvement of GABAergic and cholinergic medial septal neurons in hippocampal theta rhythm. Hippocampus *15*, 381–392.

Zaborszky, L., Pang, K., Somogyi, J., Nadasdy, Z., and Kallo, I. (1999). The basal forebrain corticopetal system revisited. Ann. N. Y. Acad. Sci. *877*, 339–367.

Zaborszky, L., van den Pol, A., and Gyengesi, E. (2012). The basal forebrain cholinergic projection system in mice. In The Mouse Nervous System, C. Watson, G. Paxinos, and L. Puelles, eds. (Elsevier), pp. 684–718.

Zemankovics, R., Káli, S., Paulsen, O., Freund, T.F., and Hájos, N. (2010). Differences in subthreshold resonance of hippocampal pyramidal cells and interneurons: the role of h-current and passive membrane characteristics. J. Physiol. *588*, 2109–2132.

Zou, X., Coyle, D., Wong-Lin, K., and Maguire, L. (2011). Computational study of Hippocampal-septal theta rhythm changes due to Beta-Amyloid-Altered ionic channels. PLoS One *6*, e21579.

Zutshi, I., Brandon, M.P., Fu, M.L., Donegan, M.L., Leutgeb, J.K., and Leutgeb, S. (2018). Hippocampal neural circuits respond to optogenetic pacing of theta frequencies by generating accelerated oscillation frequencies. Curr. Biol. *28*, 1179–1188.e3.

STAR★METHODS

KEY RESOURCES TABLE

REAGENT or RESOURCE	SOURCE	IDENTIFIER
Antibodies		
Primary antibody against PV	https://www.swant.com	PV 27
Primary antibody against Cre recombinase	https://www.biolegend.com	Cat#908002
Primary antibody against GFP	https://www.thermofisher.com	Cat#A10262
Primary antibody against choline-acetyltransferase	Umbriaco et al. (1994)	ChAT-17
Secondary antibody solution containing Alexa 488 conjugated goat anti-chicken	https://www.thermofisher.com	Cat#A11039
Secondary antibody solution containing Alexa 594 conjugated donkey anti-rabbit	https://www.jacksonimmuno.com	Cat#711585152
Secondary antibody solution containing Alexa 647 conjugated donkey anti-rabbit	https://www.jacksonimmuno.com	Cat#711605152
Bacterial and virus strains		
pAAV-EF1a-double floxed-hChR2(H134R)-EYFP-WPRE-HGHpA	https://www.addgene.org	Cat#20298
pAAV-Ef1a-DIO SwiChRca-TS-EYFP	https://www.addgene.org	Cat#55631
Chemicals, peptides, and recombinant proteins		
Urethane	https://vetcentre.com/	N/A
Fluorescent dye (1,1-Dioctadecyl-3,3,3′,3′-Tetramethylindocarbocyanine Perchlorate, DiI)	https://www.thermofisher.com	Cat#D282
Isoflurane	https://vetcentre.com/	N/A
Ketamine	https://vetcentre.com/	N/A
Xylazine	https://vetcentre.com/	N/A
Ringer's lactate solution	Local pharmacy	N/A
Betadine	Local pharmacy	N/A
Lidocaine	Local pharmacy	N/A
OptiBond XTR	https://www.kerrdental.com	N/A
Buprenorphine	http://www.richter-pharma.com/	N/A
Artificial dura	www.cambridgeneurotech.com	N/A
Eye ointment	https://www.laboratoires-thea.com	N/A
Neomycin	Local pharmacy	N/A
Paraformaldehyde	https://taab.co.uk/	Cat#P001
Xylene	Sigma-Aldrich	Cat#XX0020
DePex mounting medium	https://www.serva.de/	Cat#18243
Aqua-Poly/Mount mounting medium	https://www.polysciences.com	Cat#18606
Experimental models: Organisms/strains		
Wild type mice (C57BL/6)	https://www.jax.org/	Cat#000664
Wistar rats	https://rgd.mcw.edu/rgdweb/report/strain/main.html?id=13508588	RGD_13508588
Sst-IRES-Cre mice (C57BL/6J)	https://www.jax.org/	Cat#028864
PV-IRES-Cre mice (FVB/AntFx)	https://www.jax.org/	Cat#008069
VGAT-IRES-Cre mice (Bl6Fx)	https://www.jax.org/	Cat#016962
Vglut2-IRES-Cre (C57BL/6J)	https://www.jax.org/	Cat#028863
Software and algorithms		
OPETH	https://github.com/hangyabalazs/opeth	SCR_018022
MATLAB 2016a	https://mathworks.com	R2016a
MATLAB 2020a	https://mathworks.com	R2020a
Klustakwik spike sorting software	http://github.com/klusta-team	SCR_014480

(*Continued on next page*)

Continued

REAGENT or RESOURCE	SOURCE	IDENTIFIER
Kilosort spike sorting software	https://github.com/MouseLand/Kilosort	SCR_016422
Phy GUI	https://github.com/cortex-lab/phy	N/A
NEURON simulation environment	https://www.neuron.yale.edu/neuron/download	SCR_005393
Matlab and NEURON codes for analysis and modeling	https://github.com/hangyabalazs/ms_sync_analysis	https://doi.org/10.5281/zenodo.6798310
Matlab codes for optical tagging	https://github.com/hangyabalazs/CellBase	N/A
Matlab codes for circular statistics	https://github.com/hangyabalazs/Hangya-Matlab-code	N/A
Other		
Heating pad for rats	https://superte.ch	Cat#AHP-2
Heating pad for mice	https://superte.ch	Cat#AHP-1
Dual Ultra Precise Small Animal Stereotaxic Instrument	https://kopfinstruments.com	Cat#962
Robot Stereotaxic instrument – StereoDrive (Motorized manipulator)	https://neurostar.de	N/A
32 channel linear silicon probe	https://www.neuronexus.com	Cat#A1x32-6mm-50-177
32-channels, 4-shank Buzsáki-type acute silicon probe	https://www.neuronexus.com	Cat#Buzsaki32-A32
32-channels, 4-shank Buzsáki-type chronic silicon probe	https://www.neuronexus.com	Cat#Buzsaki32-CM32
128-channels single-shank high-density silicon probe	Fiáth et al. (2018)	N/A
DAQ module for acute rat recordings	https://www.ni.com/	Cat#PCI-6259
DAQ module for chronic mouse recordings	http://www.amplipex.com	Cat#KJE-1001
Open Ephys Acquisition Board for acute mouse recordings	https://open-ephys.org	N/A
RHD2000 Recording System	https://intantech.com	N/A
RHD USB Interface Board	https://intantech.com	Part#3100
RHD 32-channel headstage	https://intantech.com	Part#C3314
RHD 64-channel headstage	https://intantech.com	Part#C3315
RHD 6-ft (1.8 m) standard SPI interface cable	https://intantech.com	Part#3206
Optic fiber (200 μm core)	https://www.thorlabs.com	Cat#FT200UMT
Leica VT1200 vibratome	https://www.leicabiosystems.com	SCR_018453
Leica Light microscope	https://www.leica-microsystems.com	Cat#DM2500
Leica illumination force	https://www.leica-microsystems.com	Cat#SFL4000
Olympus Digital Camera (DP70)	https://americanlaboratorytrading.com	Cat#22272
Olympus Digital Camera (DP73)	https://biocompare.com	Cat#DP73

RESOURCE AVAILABILITY

Lead contact

Further information and requests for resources should be directed to and will be fulfilled by the lead contact, Balázs Hangya (hangya.balazs@koki.hu).

Materials availability

This study did not generate new unique reagents.

Data and code availability

- Electrophysiology data reported in this paper will be shared by the lead contact upon reasonable request.
- All original code has been deposited at Zenodo and is publicly available as of the date of publication. DOIs are listed in the key resources table. The GitHub repository of the code is available at https://github.com/hangyabalazs/ms_sync_analysis.
- Any additional information required to reanalyze the data reported in this paper is available from the lead contact upon request.

EXPERIMENTAL MODEL AND SUBJECT DETAILS

Wild type C57BL/6 mice (N = 11; 27.4 g ± 4.9 g, 7 males) were used for acute mouse recordings; Wistar rats (N = 7; 200–400 g; males) were used for acute rat recordings; Sst-IRES-Cre mice with C57BL/6J genetic background (N = 4; 28–30 g; males) were used for the chronic mouse recordings; 4 PV-IRES-Cre males (genetic background FVB/AntFx), 4 VGAT-IRES-Cre males (genetic background Bl6Fx) and 5 Vglut2-IRES-Cre male and female mice (genetic background C57BL/6J) were used for optogenetic tagging. All experiments were performed according to the EC Council Directive of September 22, 2010 (2010/63/EU), with all procedures being reviewed and approved by the Animal Care Committee of the Research Centre for Natural Sciences or the Institutional Animal Care and Use Committee of the Institute of Experimental Medicine and by the National Food Chain Safety Office of Hungary.

METHOD DETAILS

Surgery and electrophysiological recordings

Acute rat recordings

Rats were anesthetized with an intraperitoneal injection of urethane (40%; dose, 0.37 mL/100 g). A homeothermic heating pad connected to a rectal probe held body temperature constant (36°C). The top of the head was shaved, the rat was placed in a stereotaxic frame (David Kopf Instruments, Tujunga, US), the skin and the connective tissue above the calvaria were removed and the skull was cleared. A craniotomy was opened over the medial septum and another one over the right hippocampus. A 32-channels linear silicon probe (A1x32-6mm-50-177; NeuroNexus Technologies, Ann Arbor, US) was lowered into the right CA1 (anterior-posterior (AP): −4.5 mm and medial-lateral (ML): 3 mm) and a 32-channels Buzsaki-type silicon probe (Buzsaki32; NeuroNexus Technologies, Ann Arbor, US) was lowered to the top of the medial septum (AP: 0.4 mm and ML: −1.6 mm, 15° angle in the coronal plane). The silicon probes were dipped in red fluorescent dye (1,1′-Dioctadecyl-3,3,3′,3′-Tetramethylindocarbocyanine Perchlorate, DiI) before insertion to aid later histological reconstruction. The ground electrode was secured in the nuchal muscles.

Neural signals were acquired by two National Instruments PCI-6259 cards, amplified (2000 times) and digitized at 20 kHz. After allowing 30 min for the brain tissue around the electrode to stabilize, a 30-min recording was conducted. Theta oscillation was induced by temporarily placing an insulated clip on the tail for 1 min, repeated 3 times. After the recording, the septal probe was moved 100 μm ventrally, and the procedure was repeated. Recording sessions were conducted as long as theta oscillation could be detected via audio feedback; correct positioning of the probe in the MS was later confirmed by both histological reconstruction (Figure S1A) and the presence of theta-rhythmic neurons in the recordings.

Acute mouse recordings

Implantations were performed under general anesthesia. Mice received an intraperitoneal injection of urethane (∼1.3 mg/g). If necessary, an additional dose of urethane was injected intramuscularly to maintain the depth of the anesthesia during surgery and recordings. The body temperature of the animals was maintained during the experiments at 37°C using a thermostatically regulated heating pad (Supertech, Pécs, Hungary). Mice were placed in a stereotaxic frame (David Kopf Instruments, Tujunga, US), then the skin and the connective tissue were removed from the top of the skull. Next, two small circular craniotomies (1 mm diameter) were made on the skull with a dental drill, one for the recording probe inserted into the MS and one for the probe inserted into the hippocampus (CA1). Stereotaxic coordinates were used to determine the septal and hippocampal locations for recording (MS, AP: 0.6 mm and ML: 0.5 mm; CA1, AP: −2.2 mm and ML: 1.5 mm from the Bregma) (Paxinos et al., 2001). For post-mortem histological verification of the recording location of the probes, the backside of the silicon shank was coated with red-fluorescent dye (DiI, D-282, ∼10% in ethanol, Thermo Fischer Scientific, Waltham, US) before insertion (DiCarlo et al., 1996; Fiáth et al., 2019). The septal probe was a high-density single-shank silicon probe with 128 square-shaped recording sites (Fiáth et al., 2018). The 8-mm-long shank of the probe had a cross-section of 100 μm × 50 μm (width × thickness). The closely spaced recording sites (20 μm × 20 μm) were arranged in a 32 × 4 array with 2.5 μm spacing between the edge of electrodes. The probe was mounted on a motorized micromanipulator (Robot Stereotaxic, Neurostar, Tübingen, Germany) and inserted at a slow speed (2 μm/s) into the brain tissue to increase the single unit yield by decreasing the tissue damage (Fiáth et al., 2019). The probe was tilted at an angle of 8° from vertical in the coronal plane to have better access to the medial septum. Since the effective vertical recording area of the probe (∼0.7 mm) was smaller than the dorsoventral extent of the MS (∼1.5 mm), to obtain the spiking activity of as many septal neurons as possible, recordings were performed in three, slightly overlapping (∼0.2 mm) depths. (Unit clusters recorded twice due this overlap, based on waveform similarity and autocorrelograms, were counted only once, see below.) The hippocampal probe was a linear silicon probe with 32 recording sites and with a shank thickness of 50 μm (A1x32-6mm-50-177, NeuroNexus Technologies, Ann Arbor, US). The recording sites of the device had a diameter of 15 μm and an interelectrode distance of 50 μm. The probe was attached to a manual micromanipulator, then inserted at a speed of ∼10 μm/s to a dorsoventral depth of 2 mm. The two recording probes were connected to an electrophysiological recording system (RHD2000, Intan Technologies, Los Angeles, CA, USA) equipped with 32-channel and 64-channel headstages.

Wideband brain electrical activity (0.1–7500 Hz) was recorded on 160 channels with 16-bit resolution and at 20 kHz/channel sampling rate. A stainless-steel wire inserted into the neck muscle of the animal served as the reference and ground electrode during

recordings. Room temperature physiological saline solution was regularly dropped into the craniotomy to prevent dehydration of the brain tissue. Recordings were conducted for 15 min each, consisting of 5 min baseline period, 5 min tail-pinch-induced theta oscillation, and 5 min recovery from stimulation.

Chronic mouse recordings

Sst-IRES-Cre male mice of C57BL/6J genetic background underwent bilateral injection of AAV2/5-Ef1a-DIO-ChR2-YFP-WPRE (N = 2) or AAV5-Ef1a-DIO-SwiChRca-TS-EYFP-WPRE (N = 2) into the dorsal hippocampi (coordinates: AP -2.1 and −2.5 mm and ML ±1.5 and 1.6 mm from Bregma with tip at DV -1.2 mm from brain surface; 2 × 150–200 nL on both sides) using standard surgery techniques. Silicon probes for multichannel electrophysiological recordings were implanted above the medial septum and into the dorsal hippocampus 40–83 days after the virus injection. The surgery was performed under isoflurane anesthesia induced by ketamine-xylazine (4:1) combination diluted 6× in Ringer's lactate solution (intraperitoneal injection, dose 0.01 mL/1 g body weight). Mice were head-fixed in a stereotaxic frame (David Kopf Instruments, Tujunga, US) and their body temperature and respiratory rate were continuously monitored. After local disinfection (Betadine) and analgesia (10% Lidocaine-spray), the cranium was exposed and cleaned for application of adhesive agent (OptiBond XTR, Kerr Corporation, Orange, US). Craniotomies were performed for stereotaxis-guided implantation of a 32-channels linear type and a 32-channels, 4-shank Buzsáki-type silicon probe into the dorsal hippocampus (coordinates: AP -2.5 mm and ML + 2 mm from Bregma with tip at DV -2.1 mm from brain surface) and above the medial septum (AP +0.9 mm and ML +0.9 mm, at an angle of 12°, and with tip at DV -2.8 mm from brain surface), respectively. Both probes were mounted on a custom-made, adjustable micro-drive. The probes were coated with red fluorescent DiI for later histological confirmation of the recording site. After the recovery from the surgery, the tip of the septal probe was lowered in steps of 75–150 micrometers per day to reach the zone of cells with theta-modulated firing pattern. Within this zone, the probe was advanced in steps of 45 micrometers per day as long as the theta-modulated firing pattern was still present. In case of SwiChR-transfected animals, each shank of the septal probe was equipped with an optical fiber (50 micrometers core diameter, 0.22 NA) with tip positioned 75–100 micrometers above the uppermost recording site and glued by optical adhesive. In case of ChR2-transfected animals, one optical fiber (105 micrometers core diameter, 0.22 NA) was implanted to illuminate the fimbria, independently from the septal silicon probe. In one animal, a Buzsáki-type silicon probe was implanted into the hippocampus, instead of the linear probe. In this case, the probe was advanced stepwise to reach the pyramidal layer of the dorsal hippocampus after the post-surgery recovery period. The craniotomies were sealed with artificial dura (Cambridge NeuroTech Ltd, Cambridge, UK). The probe-micro-drive assemblies were shielded by copper mesh preventing the contamination of the recordings by environmental electric noise. The mesh was covered by dental acrylate. Two stainless steel wires inserted above the cerebellum served as ground and reference for the electrophysiological recordings. Before finishing the surgery, Buprenorphine (dose: 0.045 μg/1 g body weight) was injected subcutaneously. Recordings were started after a one-week-long post-surgery recovery and habituation to connectorization.

The electrophysiological activity was registered by a multiplexing data acquisition system (KJE-1001, Amplipex Ltd, Szeged, Hungary) at 20 kHz sampling rate. The position of the animal was tracked by a marker-based, high speed (120 frame/s) motion capture system and reconstructed in 3D (Motive, OptiTrack, NaturalPoint Inc, Corvallis, US). Recordings were conducted both in the animals' home cage (dominated by sleep) and while mice were placed on a linear track (dominated by active movement). Home cage and linear track recordings were concatenated for data analysis to include sufficient amount of time spent in theta and non-theta states. Thus, the majority of theta segments originated from movement epochs, while non-theta segments represented both quiet wakefulness and sleep. As the main focus was on general oscillatory mechanisms, these states were not subdivided further. The septal probe was lowered 45 micrometers after the recordings each day, through a total of 8–35 days of recording.

Optogenetic manipulations were carried out separately. Only the control recordings were analyzed in the present study. The Sst-IRES-Cre mouse line and the above AAV constructs were used in a large number of studies without reporting adverse phenotypic changes, and results of these studies were interpreted as general for mice and not specific for the particular strain (Adler et al., 2019; Cummings and Clem, 2020; Kim et al., 2015; Kvitsiani et al., 2013; Viney et al., 2018). Therefore, we do not consider using this particular mouse line a significant limitation of our study.

Optogenetic tagging in mice

4 PV-IRES-Cre males (genetic background FVB/AntFx), 4 VGAT-IRES-Cre males (genetic background Bl6Fx) and 5 Vglut2-IRES-Cre males and females (genetic background C57BL/6J) were used to assess the neurochemical nature of MS cells; 2 PV-Cre (n = 17, 1), 2 VGAT-Cre (n = 17, 3) and 3 VGLUT2-Cre (n = 15, 9, 6) mice yielded tagged neurons (numbers in brackets). Mice were anesthetized with an i.p. injection of ketamine-xylazine (0.166 and 0.006 mg/kg, respectively). After shaving and disinfecting (Betadine) the scalp, local anesthetic was applied (Lidocaine). Animals were positioned in the stereotaxic frame and the eyes were protected with eye ointment (Laboratories Thea). After opening the skin, the skull was cleaned and the head of the animal was leveled using Bregma, Lambda and a pair of lateral points equidistant from the sagittal suture.

A trephine hole was drilled in order to access the MS with a 10° lateral angle (MS 10°, antero-posterior +0.90 mm, lateral, 0.90 mm). An adeno-associated virus vector allowing Cre-dependent expression of channelrhodopsin2 [AAV 2/5. EF1a.Dio.hChR2(H134R)-eYFP.WPRE.hGH] was injected into the MS at 3.95, 4.45 and 5.25 mm depth from skull surface (200 nL at each depth, 100 nL at 25 nL s^{-1} and 100 nL at 5 nL s^{-1}). After the viral injections, the skin was sutured and local antibiotics (Neomycin) and analgesics (Buprenorphine 0.1 mg kg-1, s.c.) were applied.

Around two weeks after the virus injection, the animals were anesthetized with an i.p. injection of 20% urethane (Sigma-Aldrich, 0.007 mL g^{-1} body weight). The depth of anesthesia was evaluated by pinching the paw, tail, or ear of the animal, and by checking

the ocular reflex. When no reflexes were elicited, the throat was shaved, and topical lidocaine was applied. A heating pad was used to keep constant body temperature of the animals. A tracheotomy was performed in order to sustain a constant airflow (Moldestad et al., 2009). The animals were placed in a stereotaxic frame and, after opening the skin and leveling the skull, a cranial window was made above the MS (silicon probe MS 10°, antero-posterior, +0.90 mm, lateral, 0.90 mm; optic fiber MS 5° contralateral, antero-posterior, +0.90 mm, lateral, −0.50 mm), the hippocampus (silicon probe HPC, antero-posterior, −2.20 mm, lateral, 1.50 mm) and two above the cerebellum for reference electrode placement. A Neuronexus A1x32-6mm-50-177-CM32 silicon probe was placed in the hippocampus at 2.20 mm depth from skull surface. A Neuronexus Buzsaki32-H32_21 mm probe was lowered to the dorsal boundary of the MS at a 10° lateral angle (3.95 mm from skull surface). Reference electrodes for both probes were placed in the cerebellum, and a ground electrode was placed in the spinotrapezius muscle. A 200 μm core optic fiber (Thorlabs) was lowered 500 μm above the shanks of the MS probe. The MS probe and the optic fiber were lowered in consecutive recordings (100 μm steps for the probe; 50 μm steps for the optic fiber), spanning the entire depth of the MS. Extracellular data were collected by the Open Ephys data acquisition system, digitized at 30 kS/s. Each recording session consisted of an optical tagging period of two minutes, followed by a baseline period of five minutes of spontaneous activity. Three consecutive repetitions of one-minute tail pinch induced theta activity followed by one-minute control recording were applied, finishing the recording session with another two-minute-long optical tagging period. For optimizing the probability of finding tagged cells, we used the Online Peri-Event Time Histogram (OPETH) Open Ephys compatible plugin that allowed us to visualize the direct effect of the optogenetic activation at the cell population level. OPETH (Széll et al., 2020) allowed us to reduce recording time by more efficient 'hunting' for light responsive neurons in the MS and to reduce light-triggered artifacts in our recordings, improving data quality and further analysis.

Histological verification of the recording location

To detect the tracks of the silicon probes in the brain tissue, we used a histological procedure similar to that described previously (Borhegyi et al., 2004; Fiáth et al., 2018, 2019). In brief, the animal was deeply anesthetized after the recordings, then transcardially perfused with physiological saline solution followed by a fixative solution containing 4% paraformaldehyde in 0.1 M phosphate buffer (PB, pH = 7.4). Next, the fixed brain was gently removed from the skull and stored at 4°C in the fixative solution until processed further. Histological processing started by cutting 60-μm-thick coronal sections with a vibratome (Leica VT1200, Leica Microsystems, Wetzlar, Germany). Then, the brain sections were washed in 0.1 M PB, mounted onto microscopic slides and air dried. To identify brain sections containing fluorescent marks of DiI corresponding to the probe track, the slides were examined under a light microscope (Leica DM2500, Leica Microsystems) equipped with a fluorescence LED illumination source (SFL4000, Leica; Zeiss, Oberkochen, Germany in case anesthetized rats) and with a digital camera (DP70 or DP73, Olympus, Tokyo, Japan). Relevant sections from the anesthetized mouse experiments were processed for cresyl violet (Nissl) staining, dehydrated in xylene and coverslipped with DePex (SERVA Electrophoresis, Heidelberg, Germany); sections from the anesthetized rat experiments were stained for choline-acetyltransferase (ChAT; mouse monoclonal anti-ChAT (Umbriaco et al., 1994)) to visualize the MS; no staining for sections from the awake mouse experiments was performed. Finally, to verify the recording location based on the stereotaxic mouse brain atlas (Paxinos et al., 2001), sections containing the track of the silicon probe were photographed under the microscope.

Immunostaining

To verify the specificity of the ChR2 expression in targeted neuronal types in the optogenetic tagging experiments, 3 animals from each mouse strain (PV-Cre, VGAT-Cre, VGLUT2-Cre) were sacrificed 2–3 weeks after virus injection into the MS (see details in the 'Optogenetic tagging in mice' section). First, animals were anesthetized with an intraperitoneal injection of ketamine-xylazine (0.166 and 0.006 mg/kg, respectively), followed by transcardial perfusion with saline for 2 min and 4% para-formaldehyde (PFA) for 20 min. After sectioning 50 μm thick slices of the brain tissue, sections containing the MS were washed in 0.1M phosphate buffer (PB) and tris-buffered saline (TBS), then incubated in blocking medium (1% human serum albumin + 0.1% Triton-X detergent) for 1 h. Then, sections derived from PV-Cre mice were incubated in primary antibody against PV (PV 27, Swant, Switzerland), while sections from VGLUT2- and VGAT-Cre mice were incubated in primary antibody against Cre recombinase (Biologend, USA, cat#908002, 1:500) in each case mixed with primary antibody against GFP (Thermofisher Scientific, USA, cat#A10262, 1:1000) in TBS at 4°C for two days. After an extensive wash in TBS, the sections were incubated in a secondary antibody solution containing Alexa 488 conjugated goat anti-chicken (Thermofisher Scientific, USA, Cat#A11039, 1:1000), Alexa 594 conjugated donkey anti-rabbit (Jackson ImmunoResearch Europe Ltd., UK, cat#711585152, 1:500) or Alexa 647 conjugated donkey anti-rabbit (Jackson ImmunoResearch Europe Ltd., UK, cat#711605152, 1:500) antibodies at 4°C overnight. Finally, sections were mounted on slides in aqua-Poly/Mount mounting medium (cat#18606, Polysciences, Inc., USA) and images were taken with a Nikon A1R confocal microscope.

QUANTIFICATION AND STATISTICAL ANALYSIS

All signal processing codes were implemented in MATLAB 2016a and 2020a (Mathworks, Natick, US).

Hippocampal state detection

Pyramidal layer was detected from linear silicon probe recordings based on the documented phase reversal of hippocampal theta oscillation below the pyramidal layer and verified based on histological reconstruction (Figure S1C) (Buzsáki, 2006; Buzsaki et al.,

1986; Green et al., 1960). Theta detection was performed on a single channel from the stratum radiatum (400 μm below the detected pyramidal layer in rats and 250 μm below the pyramidal layer in mice), since theta amplitude was largest in this layer, allowing the most robust detection (Buzsáki, 2002, 2006). In one chronically implanted mouse, a Buzsaki-type probe was used in the hippocampus; in this case, the deepest channel was used for LFP analysis, which appeared to be below the pyramidal layer based on theta phase reversal, thus providing phase values consistent with other recordings. The appropriate theta and delta frequency band boundaries were defined separately for the three different rodent models based on the Fourier spectra of the recordings (Figure 1F). Our observations confirmed known spectral differences between urethane-anesthetized and awake rodents (frequency boundaries in anesthetized rats, delta, 0.5–2.5 Hz; theta, 3–8 Hz; in anesthetized mice, delta, 0.5–2 Hz, theta, 2–8 Hz; in awake mice, delta, 0.5–4 Hz, theta, 5–10; in optogenetic experiments, frequency boundaries were optimized for each mouse individually). Raw LFP traces were resampled at 1 kHz and bandpass filtered in the theta and delta bands using the built-in finite impulse response filter (fir1.m) with zero-phase-lag filtering (built-in filtfilt.m function). The filtered traces were Hilbert-transformed and the instantaneous amplitude and phase values were calculated as the magnitude and phase of the complex Hilbert-transform. A simple artifact removal was performed on the theta/delta ratio by clamping values exceeding 10-fold difference. Next, the theta/delta amplitude ratio was smoothed with a moving average (window size, 5 s for anesthetized and 3 s for awake recordings; the difference in window size was due to the observed faster and more frequent state transitions in awake recordings). Theta segments were defined where the theta/delta ratio exceeded an empirically defined threshold, optimized for each dataset separately (1 for anesthetized mouse and rat recordings, 2 for awake mouse recordings and 1.5 in the optogenetic experiments); all other segments were defined as non-theta. Brief interruptions of theta or non-theta segments were not considered state switches (<5 s in anesthetized and <3 s in awake recordings; the difference was due to the observed faster and more frequent state transitions in awake recordings). In some optogenetic tagging experiments (n = 8 recordings), only a part of the recording was analyzed due to electrical artifacts in other segments.

Spike sorting of septal neurons

The mouse MS recordings were fed to the Kilosort software (Pachitariu et al., 2016). Clustering was initialized with the desired number of clusters set to twice the number of channels. The Kilosort output was curated manually in the Phy template-gui graphical user interface module. We examined any potential violations of the refractory periods, slow electrode drifts, spatial distributions of action potential (AP) energies among neighboring channels, AP shapes and amplitudes and the principal components (PC) of the AP shapes. In case of noisy autocorrelograms and multiple subclusters in the PC space, we considered manual splitting of the automatically assigned cluster. The high similarity of clusters as well as lack of co-firing ('mutual refractoriness') in crosscorrelograms could imply that two automatically determined clusters belonged to the same neuron, in which case the clusters were merged. Finally, we calculated objective cluster quality measures based on the interspike interval histograms and cluster isolation distances, to verify putative single neuron clusters. Kilosort execution time was reduced by running on an Nvidia Geforce GTX 1080 graphic card with the Matlab Parallel Computing Toolbox. The anaesthetized rat recordings were clustered automatically in KlustaKwik (Rossant et al., 2016) (available at http://github.com/klusta-team) and curated manually based on auto- and crosscorrelograms similar to the mouse recordings, as described previously (Bartho et al., 2004).

In case of acute mouse recordings, the size of the probe resulted in potential overlap between subsequent recordings. Therefore, putative overlapping units were excluded by using a semi-automated method (Figure S1D). First, we calculated average spike waveforms for all clusters by averaging ±2 ms windows around all individual spike times separately for all channels. Average waveforms were aligned to zero on each channel by subtracting their mean (across time). Next, the integral of the absolute value of mean waveforms were taken for all channels as a measure of channel magnitudes. Overlapping channels from consecutive recordings were 500 μm from each other, resulting in an 88-channel displacement of the overlapping clusters due to the arrangement of the probe (4 channels in a row with 22.5 μm longitudinal separation). If two clusters shared at least 9 out of their 16 top amplitude channels, we considered them duplication candidates. Mean waveform profiles and autocorrelations were compared visually by an expert experimenter for all pairs that had been marked as duplication candidates for final decision.

Rhythmicity indices of MS neurons

Theta- and delta-rhythmicity of MS neurons was judged based on rhythmicity indices derived from autocorrelograms. First, autocorrelation of the spike train was computed in a ±3 s window at 1 ms resolution; the central peak corresponding to the total spike number was removed and the autocorrelogram was smoothed by a 20-ms moving average and normalized to an integral of 1. Next, theta and delta peaks were determined between time lags corresponding to theta and delta frequency bands. 'Peak values' were averaged from the autocorrelograms in the ±20 ms neighborhoods of the peaks. 'Baseline values' were averaged from the ±20 ms neighborhoods around the lags corresponding to half and one and a half times the peak location (assumed troughs). Finally, the difference between the peak and baseline values was normalized to the larger of the two, yielding a Theta Index and a Delta Index between −1 and 1:

$$\text{Rhythmicity Index} = (\text{peak} - \text{baseline})/\max(\text{peak}, \text{baseline})$$

Rhythmicity indices were calculated separately for hippocampal theta and non-theta segments (Figures S2A and S2B). Cells with insufficient number of spikes (<2 spikes/autocorrelogram bin on average) were excluded from later analysis.

To assess statistical significance of rhythmicity in the theta and delta frequency bands, we simulated a dataset of neurons exhibiting spiking generated by a Poisson-process. We determined the λ parameter of the Poisson-process individually for each simulated cell so that they matched the firing rate of an actual MS neuron. Rhythmicity Index was calculated for the simulated neurons using the same procedure as for the biological recordings, then Rhythmicity Index thresholds were determined corresponding to $p < 0.05$ significance levels based on this bootstrap null distribution. If both Rhythmicity Indices exceeded the threshold, rhythmicity was determined by the larger of the two Rhythmicity Indices (normalized to their respective thresholds) (Figures S2C and S2D).

Theta-burst index

To differentiate between tonically active and putative pacemaker neurons, a Theta-burst Index (TBI) was introduced, quantifying the characteristic long theta-bursts putative pacemakers fire during individual theta cycles (Borhegyi et al., 2004; Varga et al., 2008). Average autocorrelograms between lags corresponding to a pre-defined window spanning the intraburst interspike intervals (anesthetized rats, 20–40 ms; anesthetized mice, 20–50 ms and 20–40 ms in optogenetic tagging experiments, see below; freely moving mice, 10–30 ms) were normalized to the average autocorrelation, similar to the Rhythmicity Indices, providing a TBI between −1 and 1. The above windows were determined based on variations of theta frequencies across datasets. Using a traditional 20–50 ms window for all datasets altered the classification of only a few neurons and did not change the main results. Tonically active neurons were defined as those having a TBI <0 (Figures S10A–S10D).

Analysis of phase-coupling

Selected LFP channels were filtered in the theta and delta frequency bands, as described above. The filtered signals were Hilbert-transformed, and the instantaneous phase values of the analytical signal were computed. Spike phases were determined by taking the instantaneous phase values corresponding to the spike times. To quantify phase-locking, mean phase and mean resultant length (measure of phase-locking strength) were calculated as the angle and magnitude of the first trigonometric moment of spike phases. Phase value distributions for individual neurons were visualized as phase histograms, and distributions over groups of neurons were visualized as polar plots, in which each neuron was represented by a vector pointing to its mean phase, with a length corresponding to its mean resultant length and color corresponding to its firing rate in greyscale.

Crosscorrelation

Crosscorrelations of simultaneously recorded pairs of MS neurons were calculated in ±3 s windows at 1 ms resolution, smoothed by a 20-ms moving average and normalized to an integral of 1. Crosscorrelograms were aligned to their peaks between ±1.5 s and averaged both within and across rhythmicity groups.

We quantified crosscorrelation strength by taking the squared integral of mean-subtracted individual crosscorrelograms and statistically compared crosscorrelation strength within and across the major rhythmicity groups in urethane-anesthetized rats.

Pacemaker synchronization

To test how putative pacemakers synchronize during theta segments, we calculated a number of parameters and performed comparisons during theta vs. non-theta episodes. (i) Firing rates were calculated as the ratio of spike number and total segment length. (ii) Rhythmicity frequencies were estimated from the peak locations of autocorrelograms, smoothed by a 20-ms moving average (see above). (iii) Theta-bursts were defined by interspike intervals falling in the theta-burst windows defined for the TBI (see above) and average intraburst interspike intervals were computed. (iv) To estimate theta cycle skipping, an event vector was built from first spikes of bursts and single spikes. Theta cycle length was calculated for each neuron based on its rhythmicity frequency (see above), and an edge vector was defined with uniform spacing according to theta cycle length. Events were binned by the edge vector and skipping was quantified as the ratio of empty to all cycles. Although the edge vector was only based on neuronal rhythmicity and thus could not account for individual cycle variabilities, this approach likely provides a good approximation of theta cycle skipping. Since we aimed to define this metric for both theta and non-theta segments, we had to move away from LFP-based cycle definitions for this analysis. (v) Difference in rhythmicity frequency was calculated between concurrently recorded pairs of putative pacemaker neurons and normalized to the greater of the two frequencies. (vi) We compared the standard deviation of pacemaker frequency distributions during theta and non-theta segments. First, we took the difference of rhythmicity frequencies of individual putative pacemaker neurons and mean rhythmicity frequency of the recording session, to remove the variance stemming from differences in the exact theta frequency in each model (see Figure 1). We compared the absolute deviation from the mean across these normalized distributions by Wilcoxon signed-rank test.

Wavelet coherence

Spike trains of the pacemaker neurons were convolved with a 50 ms Gaussian kernel to obtain a continuous signals. Magnitude-squared wavelet coherence spectrograms of the signals were calculated around non-theta to theta transitions, where each of the segments were at least 7 s long, using the analytic Morlet wavelet.

Data analysis of the optogenetic tagging experiments

Hippocampal state detection was performed on a single channel from the stratum radiatum (~250 μm below the pyramidal layer). The LFP signal was resampled at 1 kHz. Theta and delta frequency band boundaries were determined based on spectral components (theta: 1.5–4 Hz; 1–4 and 1.5–6 Hz in 1–1 mice; delta: 0.5–1.5 Hz, 0.5–1 Hz in one mouse). Theta/delta amplitude ratio was smoothed with a 5 s window and a 1.5 threshold (1 in one mouse) was applied for theta detection. Additionally, theta amplitude was required to surpass the median value of the theta-filtered signal. Less than 5-second-long epochs were not considered as state transitions. In 8 recordings, only a part of the recording was analyzed due to electrical artifacts in other segments.

MS units were sorted in Kilosort as described above. MS neurons that had sufficient number of spikes (>500 in total and median interspike interval <500 ms) were further analyzed. Note that these spike number criteria were less stringent compared to other datasets (see above) due to generally shorter recordings. Significant photoactivation ($p < 0.01$) was determined using the stimulus-associated spike latency test (SALT) based on specific spike timing after light flashes (Kvitsiani et al., 2013). After removing the phototagging segments from the recordings, rhythmicity indices and TBI (with [20,40] ms window) were computed as described above.

Analysis of photostimulation impact

To assess the effect of phtostimulation of MS glutamatergic neurons in VGLUT2-Cre mice on CA1 oscillations, spectral power was calculated from the wavelet spectrograms for delta and theta frequency bands by averaging across within-band frequencies. Spectral power values were then averaged for the first 10 s of photostimulation and the first 10 s after photostimulation, and the theta-delta power ratio was visualized and compared statistically using Wilcoxon signed-rank test.

MS pacemaker neuron model

The model was implemented in NEURON (Carnevale and Hines, 2006). We used a fixed time step of 0.025 ms. The neuron network parameters were defined, and the simulation results were processed by Matlab scripts.

We based our model on a fast spiking single compartment neuron model by Golomb et al. (Golomb et al., 2007). This choice was motivated by the model's simplicity and its desirable firing properties, capable of high-frequency tonic firing but also rhythmic bursting, characteristic of MS pacemaker neurons. This model included a transient sodium channel (nas) that is necessary for action potential generation, the delayed rectifier potassium channel (kdr) for repolarization during fast spiking and the slowly inactivating d-type potassium channel (kd) for bursting behavior through controlling the duration of the after-hyperpolarization. We added the HCN-channel (hcn) responsible for the hyperpolarization-activated H-current, which was reported to be responsible for sag responses in MS neurons (Kocsis and Li, 2004; Morris et al., 2004; Sotty et al., 2003; Varga et al., 2008; Xu et al., 2004). We could reproduce this sag response by including the H-current (Figure 5C); we note, however, that the presence of the H-current was not a prerequisite of rhythmic bursting in the present model. Further electrophysiology data and modeling should clarify the exact channel properties of MS pacemaker neurons. Nevertheless, the present model was capable of reproducing the characteristic rhythmic bursting of MS pacemaker neurons in the range of biologically plausible rhythmicity frequencies upon current injection, serving the modeling purposes of this study.

Potential change across the cell membrane was described by the following equation.

$$C\frac{dV}{dt} = -I_{Na}(V,m,h) - I_{Kdr}(V,n) - I_{Kd}(V,a,b) - I_H(V,x) - g_L(V - V_L) + I_{app}$$

where $C = 1\mu F/cm^2$ is the membrane capacitance, $g_L = 0.1$ mS/cm^2 is the passive conductance, $V_L = -60$ mV is the equilibrium potential for leakage and I_{app} is the injected current in μA/cm^2. The lower g_L and higher V_L compared to the Golomb-model ($g_L = 0.25$ mS/cm^2, $V_L = -70$ mV) were introduced to facilitate the characteristic sag response mediated by the HCN channels. The total surface of the neuron was 5000 μm^2. The applied point source input current amplitude varied between 40 and 80 pA in the network simulations (below).

Transient Na current I_{Na} was governed by the following equations.

$$I_{Na}(V,m,h) = g_{Na}m^3h(V - V_{Na})$$

where the maximal conductance of the channels was $g_{Na} = 112.5$ mS/cm^2, the reversal potential of sodium ion was $V_{Na} = 50$ mV and the dynamics of the three activation gates m and one inactivation gate h were given by

$$\frac{dm}{dt} = [m_\infty(V) - m]/\tau_m$$

$$\frac{dh}{dt} = [h_\infty(V) - h]/\tau_h(V)$$

The time constant of the m gate was $\tau_m = 0.01$ ms and the voltage-dependent steady-state activation and inactivation variables m_∞, h_∞ and time constant of the h gate τ_h were

$$m_\infty(V) = \{1 + \exp[-(V - \theta_m)/\sigma_m]\}^{-1}$$

$$h_\infty(V) = \{1+\exp[-(V-\theta_h)/\sigma_h]\}^{-1}$$

$$\tau_h(V) = 0.5+14\times\{1+\exp[-(V-\theta_{th})/\sigma_{th}]\}^{-1}$$

where $\theta_m = -24$ mV, $\sigma_m = 11.5$ mV, $\theta_h = -58.3$ mV, $\sigma_h = -6.7$ mV, $\theta_{th} = -60$ mV and $\sigma_{th} = -12$ mV.

The delayed rectifier K current I_{Kdr} was governed by

$$I_{Kdr}(V,n) = g_{Kdr}n^2(V)(V-V_K)$$

where the maximal conductance of the channels was $g_{Kdr} = 225$ mS/cm^2, the reversal potential of potassium ions was $V_K = -90$ mV and the dynamics of the two activation gates n were defined by

$$\frac{dn}{dt} = [n_\infty(V) - n]/\tau_n(V)$$

The voltage-dependent steady-state activation variable n_∞ and time constant of the n gates τ_n were

$$n_\infty(V) = \{1+\exp[-(V-\theta_n)/\sigma_n]\}^{-1}$$

$$\tau_n(V) = \left\{0.087 + 11.4\times\left\{1+\exp\left[\frac{V+14.6}{8.6}\right]\right\}^{-1}\right\} \times \left\{0.087 + 11.4\times\left\{1+\exp\left[\frac{-(V-1.3)}{18.7}\right]\right\}^{-1}\right\}$$

where $\theta_n = -12.4$ mV, $\sigma_n = 6.8$ mV.

The slowly inactivating d-type K current I_{Kd} was governed by

$$I_{Kd}(V,a,b) = g_{Kd}a^3b(V-V_K)$$

where the maximal conductance of the channels was $g_{Kd} = 1.8$ mS/cm^2 and the dynamics of the three activation gates a and one inactivation gate b were defined by

$$\frac{da}{dt} = [a_\infty(V) - a]/\tau_a$$

$$\frac{db}{dt} = [b_\infty(V) - b]/\tau_b$$

The time constant of the activation gate was $\tau_a = 2$ ms and that of the inactivation gate was $\tau_b = 120$ ms. The voltage-dependent steady-state activation and inactivation variables a_∞ and b_∞ were

$$a_\infty(V) = \{1+\exp[-(V-\theta_a)/\sigma_a]\}^{-1}$$

$$b_\infty(V) = \{1+\exp[-(V-\theta_b)/\sigma_b]\}^{-1}$$

where $\theta_a = -50$ mV, $\sigma_a = 20$ mV, $\theta_b = -60$ mV, $\sigma_b = -6$ mV.

We introduced smaller τ_b compared to the Golomb-model (where τ_b was 150 ms), which resulted in faster rhythmicity that was within the delta-theta frequency range. We used a θ_b of -60 mV that enabled the characteristic sag response by the H-current.

To define the HCN channel, we started from a generic HCN model by Kali and Zemankovics (Káli and Zemankovics, 2012) which used an alternative parameterization of the Hodgkin-Huxley type model as described by Borg-Graham (Borg-Graham, 1999). Next, parameters of our model were tuned to match the dynamical properties of the H-current in MS neurons (Migliore and Migliore, 2012; Xu et al., 2004). The final I_H current was defined by

$$I_H(V,x) = g_Hx(V-V_H)$$

where the maximal conductance of the channels was $g_H = 0.1$ mS/cm^2 and the reversal potential of the cations was $V_x = -30$ mV. The open probability of the activation gate x evolved as

$$\frac{dx}{dt} = [x_\infty(V) - x]/\tau_x(V)$$

where the voltage-dependent steady-state activation variable x_∞ and time constant τ_x were

$$x_\infty(V) = \{1 + exp[-(V - \theta_x)/\sigma_x]\}^{-1}$$

$$\tau_x(V) = \left\{ G_x exp\left[\frac{\gamma_x(V - \theta_x)}{\sigma_x}\right] + G_x exp\left[\frac{(\gamma_x - 1)(V - \theta_x)}{\sigma_x}\right] \right\}^{-1} + \tau_{x0}$$

where rate coefficient was G_x = 1.2353 1/ms, asymmetry parameter was γ_x = 0.81, half activation was θ_x = −98 mV, σ_x = −6.73 mV, τ_{x0} = 130 ms.

Modeling the MS pacemaker network

The neuron network parameters were defined, and the simulation results were processed in Matlab. In our network simulations, 20 inhibitory pacemaker neurons were connected at an average connection rate (CR) varied between 0 and 100% (randomly chosen connections were deleted from a fully connected graph). Inhibitory synapses were implemented with the built-in Netcon() and ExpSyn() point processes of the NEURON environment. Netcon() implements a presynaptic source object with threshold, delay and weight parameters. The threshold parameter was fixed at 0 mV. Synaptic delays between 1 and 15 ms (1, 4, 7, 11, 15 ms) were tested (Figures S14A–S14E), fixed at 7 ms with 10% variance for simulations shown in Figure 5 and S14F–S14K. Expsyn() modelled the postsynaptic effect with a discontinuous change in conductance after each incoming spike event (which was initiated by Netcon() when the presynaptic membrane potential crossed the spike detection threshold), followed by an exponential decay with time constant τ:

$$I(t, V) = g(t) \times (V - e)$$

$$g(t) = weight \times \exp(-t/\tau)$$

where I (in nA) was the current transmitted to the postsynaptic cell, g (in μS) was the actual conductance, *weight* (in μS) was the maximal conductance or synaptic strength, e (in mV) was the reversal potential, which was set to −70 mV and τ (in ms) was the exponential decay factor, which was set to 2 ms with 10% variance.

The network simulations were implemented by NEURONS's built-in IClamp() function, which simulated an electrode delivering current pulses of a given duration, amplitude and delay. Every neuron received three electrodes at their somata, delivering a sequence of three current pulses implementing weak, strong (1.4-fold), and weak tonic excitation in this order, with variable stimulus onset latency uniformly dispersed over a one-second-long interval to avoid synchronous phase reset across the population. The extent of increase in excitation strength was based on the average firing rate increase of MS glutamatergic neurons (Figure 6V), the main excitatory input to MS GABAergic cells (Hajszan et al., 2004), determined by our optogenetic tagging experiments. During each simulation, synaptic and stimulation parameters were drawn from normal distributions with given mean and variance.

We modeled the theoretical output signal of the simulated pacemaker network as a proxy for the septal input to the hippocampus. Spike trains (i.e. the events when the simulated membrane potential reached the 0 mV spike generation threshold) were convolved with a 50 ms Gaussian window and averaged across all neurons. State detection was executed similarly as described for real data above with the following parameters: resampling rate, 1 kHz; theta band, 4–6 Hz; delta band, 0.5–4 Hz; theta-delta ratio was smoothed, and short segments (<0.5 s) were handled as above; theta-delta ratio threshold, 2.

Exploring the parameter space of the pacemaker network model

To study the network dynamics and its dependence on key parameters, we performed a series of simulations. In each run, we simulated a 5-second-long baseline period, followed by a 10-second-long 'expected theta' period when a stronger excitatory current was injected to all pacemaker neurons (1.4-fold of baseline), followed by a 5-second-long 'expected non-theta' period when tonic excitation was reverted to baseline (with varied stimulus onset latency, see above). We systematically varied the connection rate (0–100% in increments of 20%), mean synaptic delay (1, 4, 7, 11, 15 ms), mean absolute synaptic strength (1, 3, 6, 9, 12 nS), mean (40–80 pA in increments of 10 pA) and variance (0–20% in increments of 5%) of baseline stimulation strength. The variance of synaptic weights, delays and decay times was kept at 10%.

We performed three sets of simulations. First, the variance of baseline stimulation was fixed at 10% and the synaptic delay at 7 ms, while all combinations of connection rates, stimulation strength and synaptic weight were tested (Figures S14A–S14C). Second, stimulation strength was fixed at 60 pA, synaptic weight at 3 nS and stimulation variance at 10%, while all possible combinations of connection rate and synaptic delay were tested (Figure S14D). Third, stimulation strength was fixed at 60 pA, synaptic weight at 3 nS and synaptic delay at 7 ms, while all possible combinations of connection rate and variance of stimulation strength were tested (Figure S14E). We repeated each simulation for a given parameter arrangement 10 times by redrawing parameters from the same distributions, performing 1800, 300 and 300 runs in the first, second and third set of simulations, respectively. We evaluated the simulated models by calculating a simple synchronization score, which quantified the ratio of the total simulation time the network spent in the expected state based on the state detection described above.

Model network synchronization

Based on the exploration of the network model parameter space, we fixed mean baseline excitation at 60 pA with 10% variance, connectivity rate at 60%, mean synaptic strength at 3 nS and mean synaptic delay at 7 ms. We performed a series of simulations (n = 60) of 60-second-long segments, with 20 s of baseline, followed by 20 s of increased excitation (with varied stimulus onset latency, see above), followed by 20 s of returning to baseline excitation levels to enable large scale analysis of pacemaker synchronization (Figures 5F and S14F–S14K). Rhythmicity indices, TBI (theta-burst interspike interval window, 20–40 ms), significant modulations, phase preference (with respect to the theoretical population output) and pacemaker synchronization were computed as described for the biological data.

We detected anti-phasic firing based on the peak location distributions of pairwise cross-correlations between pacemaker neurons in the model, since anti-phasic firing results in the over-representation of cross-correlation peaks around half of the cycle length of theta. We ran a parameter search to detect such over-representations by defining an in-phase and an anti-phase sync score for each simulation. Crosscorrelogram peaks during the stronger tonic input period (6–15 s) were detected in the −300 to 300 ms range of lags, looking for peaks at least 166.7 ms apart (corresponding to maximal theta frequency). Crosscorrelogram 'offset' was defined as the lag corresponding to the peak that was closest to zero. Next, histograms of absolute offsets were calculated using a bin size of 25 ms. The 'in-phase' score was defined as the value of the first offset bin, while the 'anti-phase' value was defined as the fourth offset bin, corresponding to anti-phase crosscorrelation lags.

Statistical testing

Significant rhythmic firing rate modulation was determined by a bootstrap permutation test at a $p = 0.05$ significance level as described above. This provides a conservative threshold for rhythmicity, constrained by the sample size (number of recorded action potentials per neurons), as indicated by the apparent presence of rhythmic modulation beyond the thresholds in Figure S2D. Please note that this is only apparent in the Rhythmicity Index-sorted images that allow pattern-detection across multiple neurons.

We used non-parametric tests for comparing central tendencies of distributions: Mann-Whitney U-test for non-paired and Wilcoxon signed-rank test for paired samples. We report W+ test statistic (ranksum for theta- > delta-related measures for theta-delta comparisons). Nonparametric tests are ideally suited when no assumptions on underlying distributions are made. We avoided statistical tests that require normal distribution of the underlying random variables, since statistical tests for normality may reject the null hypothesis of the Gaussian distribution of data, but the lack of significance does not prove normality, and their statistical power strongly depends on sample size. Additionally, firing rates are positive random variables known to deviate from normal distribution (Buzsáki and Mizuseki, 2014). Significance was determined at $p < 0.05$ (*), $p < 0.01$ (**) and $p < 0.001$ (***), as also indicated in the figure legends.

We considered multiple circular statistical models to explain the distribution of mean theta phase values of the putative pacemaker neurons. These models were mixtures of one to five von Mises distributions (circular analog of the Gaussian distribution), corresponding to unimodal, bimodal, trimodal, etc. distributions on the circle (Fisher, 1993). To assess which model described the data best, we performed model selection by calculating Akaike Information Criterion (AIC) and Bayesian Information Criterion (BIC) for these models. The model with the lowest value corresponded to the best fitting model (Akaike, 1973; Brewer et al., 2016; Konishi and Kitagawa, 2008). The information criteria did not support models with more than three modes; therefore, we focus on the unimodal, bimodal and trimodal phase distributions below. For the anesthetized rat recordings, we found that AIC values for the unimodal, bimodal and trimodal distributions were 109.08, 103.19 and 108.98, respectively. The BIC values were 111.81, 110.03 and 119.92; thus, both information criteria indicated that the bimodal phase distribution described the data best. This was further confirmed by a parametric bootstrap approach (Fisher, 1993), which statistically tested whether a unimodal or a bimodal model can be rejected based on the data. The unimodal hypothesis was rejected at $p = 0.02$, while the bimodal hypothesis could not be rejected ($p = 0.91$). The mean phases of the best fitting mixture of two von Mises distributions were 147.28° and 342.57° (referenced to pyramidal layer theta). Model selection results in mice favored either a unimodal (AIC in freely moving mice: 111.17, 113.11, 111.67; BIC in freely moving mice: 114.28, 120.89, 124.11; BIC in anesthetized mice, 171.09, 180.66, 175.92 for the unimodal, bimodal and trimodal distributions, respectively) or a more complex trimodal (AIC in anesthetized mice: 167.39, 171.41, 161.12 for the unimodal, bimodal and trimodal distributions, respectively) phase model.